Ex-Vivo 3D Assessment of Carotid Stenosis with Ultrasound

by

Kathie L. Dionisio

B.S. Biomedical Engineering
Columbia University School of Engineering and Applied Science, 2003

Submitted to the Department of Mechanical Engineering
in Partial Fulfillment of the Requirements for the
Degree of

Master of Science in Mechanical Engineering
at the
Massachusetts Institute of Technology

June, 2005

Signature of Author_____
Department of Mechanical Engineering
June 2, 2005

Certified by_____
Dr. Robert S. Lees, Professor
Harvard-MIT Division of Health Sciences and Technology
Co-Thesis Supervisor

Certified by___
Dr. Raymond C. Chan, Instructor
Department of Radiology
Co-Thesis Supervisor

Certified by_____
Dr. Roger D. Kamm, Professor
Department of Mechanical Engineering and Biological Engineering Division
Thesis Reader

Accepted by_____
Dr. Lallit Anand, Professor
Department of Mechanical Engineering
Chairman, Department Committee on Graduate Students

Ex-Vivo 3D Assessment of Carotid Stenosis with Ultrasound

by

Kathie L. Dionisio

Submitted to the Department of Mechanical Engineering
on June 2, 2005 in Partial Fulfillment of the
Requirements for the Degree of
Master of Science in Mechanical Engineering

ABSTRACT

Atherosclerosis causes heterogeneous remodeling of arterial structure and composition in the carotid vessel wall. It has been shown that the progression of the disease can be monitored by tracking changes in the carotid intima-media thickness (IMT). Non-invasive peripheral vascular ultrasound (U/S) of the carotid artery is a non-invasive, cost effective, accepted means of measuring IMT.

Traditionally, evaluation of IMT in the carotid has been limited to 2D U/S scans. This method is disadvantageous as 2D scans are scan plane dependent, limiting the area over which one can evaluate the extent of the disease. Reproducing the identical scan plane on subsequent scans is also difficult. Evaluation of the carotid vessel wall in 3D will allow for a more complete and reproducible assessment of disease through IMT measurements.

We have constructed a fully 3D image processing scheme for analyzing carotid U/S volumes to extract the inner and outer vessel wall boundaries. Sequences of 2D B-mode U/S cross sections of ex-vivo carotid specimens are collected and voxelized to create 3D U/S volumes. By applying a 3D directionally sensitive, edge preserving filter to the U/S volumes, we obtain 3D edge fields that are more distinct than traditional gradient edge fields. Initial point selection of the boundaries, together with these enhanced 3D edge fields, are used with a deformable surface to extract the final inner and outer vessel boundaries. Through intra- and inter-observer tests on IMT differences, we show that the 3D boundaries extracted using our automatic technique are more reproducible than boundaries extracted from manual point selection.

Thesis Co-Supervisors: Dr. Robert S. Lees and Dr. Raymond C. Chan

Acknowledgments

Graduate school is intellectually stimulating, exciting, and adventurous, yet at times it can also be cruel. The support of my friends and family was indispensable over the past two years, and played an integral part in this thesis being seen through to completion.

To my Columbia crew – I'm still wondering whether I should take the salt or the pepper route in life... To EC405, for the reunion weekends that invigorated me. To Kevin, for being the first big brother I always wanted but never had. To L, Kira, and Sas, for keeping me continuously entertained via email with your stories.

To the MIT crew, who have made the graduate school experience more enjoyable than I ever could have hoped for... To Dave, for being the second big brother I always wanted but never had. To Robin, for sharing her southern-cooking recipes. To Melinda, for always being a calming presence. To Mike, for reminding me that no matter how bad things get, at least I am not sleeping in a hole. To Adam, for having faith that I can conquer any new adventure he brings me on, and for always bringing me home alive from said adventures. To Pete, for being someone I can look up to. The fact that you are so pulled together, yet still change your life plans every week is more reassuring than you could know. To Mo, for supporting me through the quals process, twice - I couldn't have done it without you. To the combined households of the Mother Country and the Garden, for always welcoming me into their houses to sleep on their couches and clean up after parties. To Stigma, for giving me something to look forward to during this grueling last semester, and for giving me the opportunity to work on a project I am thoroughly excited for and passionate about. To Eric, Tim, Devon, Jim, and Brian, for showing me the good that is the Thirsty. To Tiffany, Sara, and Lucy, whom I can always count on for an eventful night out.

To my family, for always giving me unwavering support in whatever I choose to do. Thank you to my parents for welcoming, feeding, and providing a home away from home for dozens of graduate students over the past two years. I promise I will be careful in Africa! A special thanks to Karyn, my "inexperienced observer," for contributing an essential part of this thesis. I wouldn't have half of my results if it weren't for your point selections.

Lastly, to my advisors, without whom this research never would have been completed.

To Dr. Bob, who early in my career at MIT said to me "Who said slavery was abolished? We still have graduate students." To Ray, to whom I owe an enormous thank you for the work you put in leading me through each step of this thesis. I will never keep all back-up copies of my data in the same bag. To Jean, Lee, Dianne, Brenda, Marie, and Dr. Hemphill, for your technical assistance, administrative help, and clinical expertise.

Contents

Chapter 1

Background

1.1 Introduction and Motivation

While cancer has recently surpassed heart disease as the leading cause of death for individuals younger than 85 [1], cardiovascular disease is still the leading cause of death in the developed world, causing ~60% of deaths [2]. Atherosclerosis is the most prevalent form of cardiovascular disease. The slow progression of carotid atherosclerosis provides us with a window of opportunity to halt progression of the disease before an acute clinical event occurs. Because of narrowing of the lumen, atherosclerosis causes a decrease in blood flow downstream from plaques. Also, weakening of vessel walls from structural remodeling can lead to dilation or rupture, which can cause stroke or heart attack. Techniques for detecting atherosclerosis in the early stages are desirable as measures can then be taken to halt its progression.

Currently, clinical methods for evaluating carotid intima-media thickness (IMT) focus on measurements from 2D B-mode ultrasound scans [3]. B-mode ultrasound (U/S) provides us with a non-invasive, cost effective technique for evaluating IMT. Many clinicians rely on manual identification of vessel wall boundaries on U/S images to determine IMT however a more reproducible method of boundary extraction is desirable. Since atherosclerosis causes heterogeneous remodeling of arterial structure and composition in the carotid vessel wall, extension of current methods to 3D is crucial. 2D scans are scan plane dependent, limiting the area over which one can evaluate the progression of disease; 3D evaluation allows us to more completely characterize disease in a patient.

Our goals include the development of a reproducible method for 3D carotid morphology estimation, to allow clinicians to accurately track changes in the intima-media thickness early on and begin treatment for the patient at an earlier stage of the disease.

1.2 Pathogenesis

Atherosclerosis is a process in which fatty substances, cholesterol, cellular waste products, calcium, and other substances collect in the inner lining of the arterial wall to form plaques [4-5]. As cells and cellular waste build up, the arterial wall thickens. Atherosclerosis is characterized by a thickening and a decrease in elasticity of the vessel wall [6].

The carotid arteries are the main source of blood supply to the brain. Tracking and treating disease in the carotid artery is crucial as atherosclerosis can narrow or completely obstruct the vessel, decreasing blood flow downstream from a plaque [6]. This elastic artery has an internal diameter of 0.2-0.8 cm, and is 10-20 cm in length [7]. The carotid artery consists of three concentrically arranged layers. The thin intima is the layer of the vessel wall adjacent to the lumen. The internal elastic lamina separates the intima from the media, the middle layer in the carotid vessel wall. The media is composed of elastin and collagen, along with layers of smooth muscle cells. The outermost layer of the carotid vessel wall is the adventitia, mostly composed of connective tissue [6].

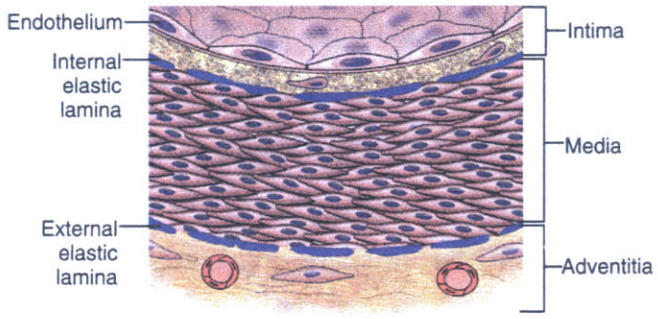

Figure 1-1. Layers of the carotid vessel wall [6].

Atherosclerosis develops as a response to one of several kinds of injury to the endothelium. A number of factors are known to put an individual at a higher risk for

cardiovascular disease. These include uncontrollable factors, such as sex and age, and controllable factors, such as high cholesterol, smoking, and obesity. Studies have shown that males, the elderly, and individuals with a family history of premature cardiovascular disease are at a much higher risk. There are also a number of controllable factors which can contribute to progression of atherosclerosis. High blood pressure, (>140/90 mm Hg), is a risk factor as high blood pressure causes the heart to work harder than normal, as a result the heart enlarges and weakens over time, which makes the heart and arteries more prone to injury. High levels of low density lipoprotein (LDL >160 mg/dL), low levels of high density lipoprotein (HDL <40 mg/dL), and high levels of triglycerides (>200 mg/dL) can all contribute to the progression of atherosclerosis. Smoking is thought to exacerbate the disease, as the amount of oxygen in the blood is reduced, causing damage to the vessel walls. Tobacco smoke is also thought to lower HDL levels in the blood. Diabetes mellitus, obesity, and physical inactivity are also known risk factors for the disease [5].

After initial damage to the vessel wall, in the early stages of atherosclerosis, we see an inflammatory response [8-10]. There is an increased permeability to fluids and swelling in the vessel wall. Monocytes and lymphocytes migrate into the arterial wall from the blood in response to the inflammation. Monocytes accumulate lipid and become macrophages, and together with the lymphocytes accumulate in the intima to form a fatty streak. As the lymphocytes, macrophages, and smooth muscle cells proliferate, the fatty streaks develop into plaques containing a lipid core, and covered by a fibrous cap [11-13].

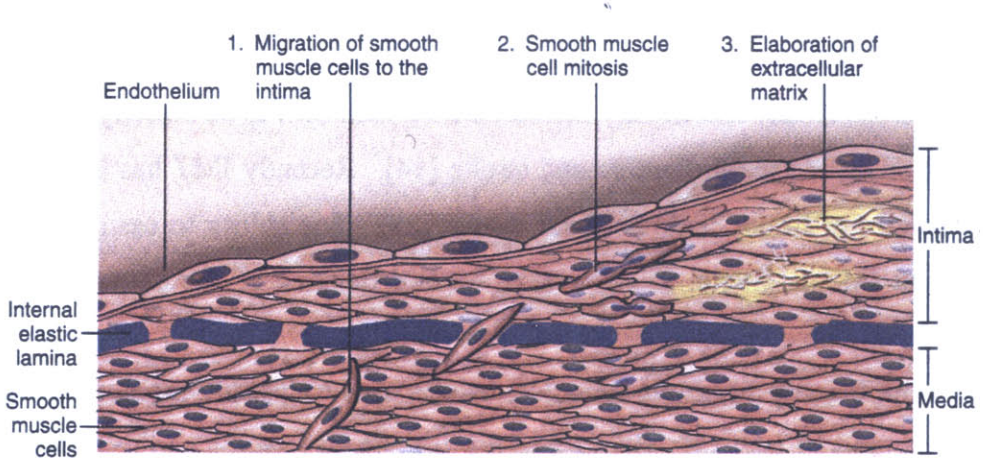

Figure 1-2. Mechanism for intimal thickening [6].

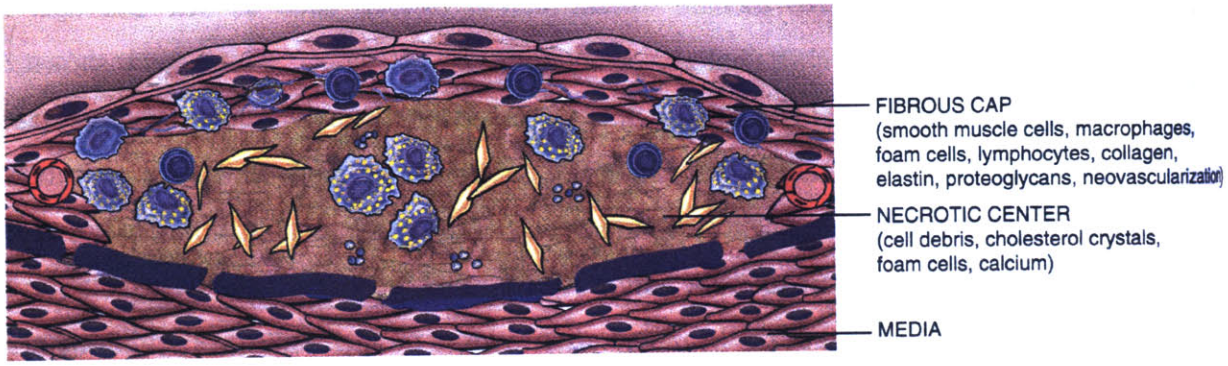

Figure 1-3. Components of an atheromatous plaque, including fibrous plaque and necrotic center [6].

These fibrous plaques are composed of layers of macrophages and smooth muscle cells and can protrude into the lumen, occluding blood flow through the artery [11-13]. Growth of the lesion can decrease blood flow downstream. Problems can also occur if the fibrous plaque ruptures and blood clots block vessels leading to the heart or brain, causing heart attack or stroke respectively. Another result of the build up of macrophages and lymphocytes is their production of proteolytic enzymes that degrade structural elements in the wall. Meanwhile, the macrophage-mediated degradation of the elastin and collagen structural elements of the vessel wall weakens the arterial wall.

1.3 Ultrasound to Evaluate Atherosclerosis

Carotid intima-media thickness has been shown to correlate with cardiovascular risk factors, and the presence of cardiovascular disease. Increases in carotid IMT are a marker of underlying atherosclerosis, specifically increased IMT is known to be directly associated with an increased risk of myocardial infarction and stroke [14]. Recently IMT has been shown to be a powerful predictor of future cardiovascular events [15]. The ability to easily and reproducibly evaluate carotid IMT is crucial to the evaluation and tracking of the extent of cardiovascular disease in patients.

Real time B-mode ultrasound imaging can be used to directly measure the intima-media thickness of the arterial wall [3]. Because of the superficial location and minimal movement of the carotid artery, U/S provides a non-ionizing, low energy, non-invasive, cost-effective imaging

technique that can be used to track changes in IMT. For this reason, U/S evaluation to measure changes in IMT is frequently used as a surrogate endpoint in clinical trials of anti-atherosclerotic therapy [16].

1.4 3D versus 2D

Three-dimensional ex-vivo carotid specimens and in-vivo carotid arteries pose challenges when evaluated in 2D. The heterogeneous composition and varying IMT of the carotid artery can be better evaluated in 3D versus 2D. When an observer evaluates 2D images of a 3D carotid they can not appreciate the full extent of disease. Multiple 2D snapshots can be taken over the length of the artery, however the technician then must mentally process the 2D information to interpret the results in 3D. This can be a very time consuming and subjective process, and is also highly operator dependent. If a 3D image of the artery can be objectively created by a computer, we eliminate the subjective step associated with the technician interpreting the 2D images. Also, when volume measurements of the arterial wall are required, assumptions must be made to obtain these 3D measurements from a sequence of 2D images, which could introduce a large margin of error in the final results. With 3D images, one can calculate any 3D measurement of the specimen directly, without any assumptions about geometry or location of the specimen [17].

A low level of reproducibility is a disadvantage of 2D U/S images which is nearly eliminated with 3D U/S volumes. The 2D U/S images represent one plane of interest at an arbitrary angle in the body, and it is very difficult to reproduce the exact location of the image at a later date for follow-up testing and measurements. With 3D images, the entire volume of interest can be reproduced and compared to a reconstructed volume from a previous time point, eliminating the need to identically reproduce one image location. Following from this fact, when evaluating a patient versus an ex-vivo specimen, there are limitations on the 2D U/S image views which can be obtained because of the anatomy of the patient. When we reconstruct a 3D volume, we can reslice the volume at any angle, thus allowing the technician to see views of the patient's anatomy that could not be otherwise obtained [18]

Currently, U/S machines use transducers with a 1D array to collect 2D images. Transducers containing 2D arrays which would allow collection of fully 3D U/S images are

currently being developed, but are only in their early stages. The machines do not yet have sufficient resolution capabilities to image the thickness of the vessel wall. At this time, to obtain 3D U/S images, multiple 2D U/S images covering the area of interest must be collected, along with accurate readings of the position and orientation of the transducer at each location an image is captured [19]. Position and orientation information is combined with the 2D U/S images to create a 3D volume to process. The two most common ways of collecting the 2D images and position information are through mechanical translation or freehand translation of the transducer with an attached position sensor.

When mechanical translation is utilized, a commercial linear and/or rotational motion device is used to translate the transducer as the 2D U/S images are captured. The mechanical translators come in two varieties, an internal device that incorporates the "guts" of the transducer within the mechanical translation apparatus, and an external device that can fit around and accommodate a conventional transducer. The advantages of mechanical translation devices are that they allow for exact movements of the transducer so that the location of the transducer during scanning is precisely known. However, the apparatus can be bulky and heavy, limiting the scans which can be done based on the anatomy of the patient or the size of the specimen. Also, internal devices may require a specific U/S machine, a large additional expense if your facility does not have the correct machine. While external devices may be compatible with many different U/S machines, they may need to be adapted for each scan depending on the size and shape of the person or specimen. This process can be time consuming and potentially costly [18].

With freehand translation of the U/S transducer, some of the problems associated with mechanical translation are eliminated however others are introduced. With freehand translation, a position sensor is used to detect and record the position and orientation of the transducer during scanning through a receiver secured to the transducer. A common position sensor used is a magnetic field sensor with six degrees of freedom.

Figure 1-4. Magnetic field sensor for motion tracking.

With this device a transmitter is mounted close to the specimen or person being scanned. The transmitter produces a spatially varying magnetic field that is measured by an electromagnetic receiver mounted on the U/S transducer. The receiver contains three perpendicular coils that sense magnetic field strength and measure it at three different points relative to the fixed transmitter. This allows the technician to sweep the transducer over the specimen of interest while the main unit records information to calculate the position and orientation of the transducer at each moment that an image is recorded. The advantages of freehand translation over mechanical translation are that a position sensor can be added to most existing 2D U/S machine with relatively low additional expense and effort. Also, in freehand translation the only adaptation to the U/S transducer is the addition of a small, unobtrusive receiver that will not place any additional constraints on the positioning of the transducer. External and internal mechanical translation devices are disadvantageous as they can interfere with the range of motion of the transducer during scanning.

With freehand translation the scanning path and thus transducer positions are not predefined as they are with mechanical translation. The flexibility in the range of motion of the transducer can be an advantage of freehand translation if the technician ensures that images are recorded rapidly enough to obtain a dense sampling of images that span the entire volume of interest. This can be easily accomplished with some practice with the speed of translation and positioning of the transducer during scanning.

Another disadvantage of freehand translation is the potential error introduced by the position sensor. If a magnetic field sensor is used, care must be taken to ensure that

electromagnetic fields from other pieces of equipment in the vicinity of the U/S machine are minimized so that the external electromagnetic fields do not interfere with the electromagnetic field being used to calculate the position of the transducer. The position sensor must also be calibrated so that the error in position measurements is known, and can be shown to be insignificant relative to the experimental measurements [18].

After the series of 2D U/S images and corresponding position information has been collected, each pixel in the 2D images is aligned in its correct position relative to each other pixel based on the readings from the position sensor. An equivalent 3D volume is then created from these pixel intensities. There are two main methods used for 3D image reconstruction, feature based reconstruction and voxel based reconstruction. In feature based reconstruction, the boundaries of interest are extracted from each 2D image and the 3D volume is created based on the extracted boundaries. This technique is advantageous because of its fast computation time, since 3D surfaces are created based only on the boundaries extracted in 2D. However, this can also be a disadvantage of the technique as subtle features and tissue texture can be lost in the process. Lastly, manual boundary extraction can be time consuming, while automatic boundary extraction is subject to errors.

In voxel based reconstruction, after the 2D images are correctly aligned relative to each other, each individual pixel can be assigned a 3D position in the coordinate system of the new volume. Intensities are assigned to each voxel position in the reconstructed volume based on interpolation of the pixel values from each 2D image. Advantages of voxel-based reconstruction are that once the 3D volume is constructed, the volume can be re-sliced so that new views can be seen which may not have been visible in the 2D images. Also, voxel-based reconstruction preserves all of the original information from the 2D images, so the original images can be voxelized as many times as necessary to achieve the final result desired. A disadvantage of preserving all original image information is that the size of the data files increase significantly because of the large number of 2D images necessary to create the 3D volume. Lastly, one must take note of the density of the 2D images over the range of the 3D volume created, as large gaps between 2D images will contribute to inaccuracies in interpolation [18].

There are many potential sources of error in 3D volume reconstruction. A broad category are those which come about because of errors in the position readings associated with each 2D image. These can occur with a magnetic field position sensor when electromagnetic fields from

other sources interfere with the magnetic field position sensor. One must ensure that the area surrounding the magnetic field position sensor contains minimal amounts of metal and electrical interference from CRT monitors, ac power cables, and other electronic devices. Another source of error can be introduced if the 2D images collected do not reflect a full sampling of the volume region of interest. This can occur if the transducer is translated too quickly over the volume, or if the image capture rate is too low.

Chapter 2

Data Acquisition

2.1 Hardware

Ultrasound machine

A broadband 5-12 MHz peripheral vascular transducer of a Philips HDI 5000 Sono CT machine (ATL-Philips Ltd., Bothell, WA) was used to scan the specimens and capture the B-mode U/S images.

Figure 2-1. Philips HDI 5000 Sono CT Ultrasound.

Flock of Birds

To obtain position and orientation readings for each 2D U/S frame recorded, the Flock of Birds (Ascension Technologies Inc., Burlington, VT) was used. The Flock of Birds is a 6 degree of freedom measuring device which outputs 3 position readings and 3 orientation readings each time a measurement is requested. The device consists of a fixed transmitter and a receiver, both connected to the main unit of the device. The main unit is also connected to a computer, and coordinates the communication between the transmitter, the receiver, and the computer. The transmitter, which we have mounted on a wooden table, transmits a pulsed DC magnetic field which is picked up by the receiver attached to the U/S transducer. The receiver measures the magnetic field emitted by the transmitter and computes the position and orientation of the transducer at any time based on the measured magnetic field. The Flock of Birds outputs the X, Y, and Z position coordinates and orientation angles of the sensor with respect to the transmitter. Orientation angles are defined as rotations about the X, Y, and Z axes as defined by the transmitter.

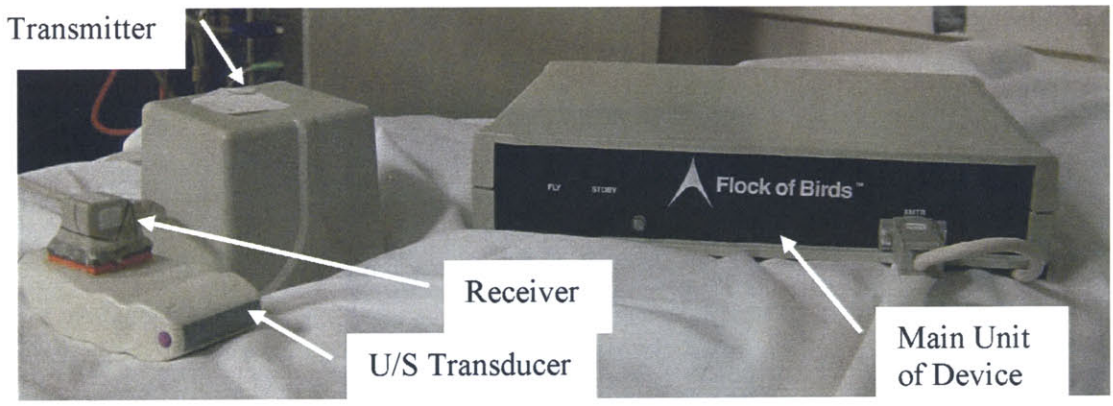

Figure 2-2. Ascension Technology Flock of Birds magnetic position sensor.

Manometer

An Artisan MP2000.001 digital manometer (APT Instruments, Litchfield, IL) was used to monitor the internal carotid pressure during scanning. The MP2000.001 has a response time of 0.3 msec, and an operating range of 0-5 psig, with an accuracy of +/- 0.3% of full scale at 25°C. Artisan Data Collection Software was used to record the internal carotid pressure during each second of scanning.

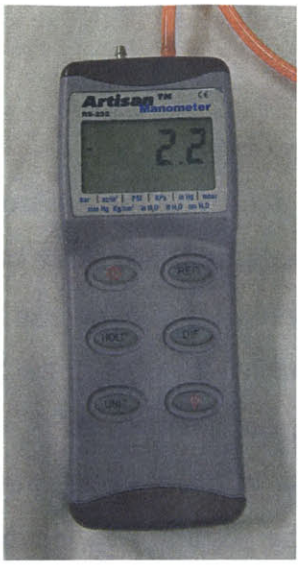

Figure 2-3. Artisan MP2000.001 digital manometer.

2.2 Software

Stradx

Stradx V.7.2 (Cambridge University, UK) software developed by Richard Prager, Andrew Gee, and Graham Treece of the Machine Intelligence Laboratory at Cambridge University was used to capture and voxelize the 2D U/S images. This free software allows the user to capture 2D U/S images along with corresponding 3D position information obtained from a Flock of Birds. The data can then be voxelized to create a 3D volume of the specimen being scanned.

Matlab

After voxelization of the 2D U/S images, all image processing was done in MATLAB V6.5, release 13, from The MathWorks, Inc. (Natick, Massachusetts).

Dataplot

Dataplot open source software from the National Institute of Standards and Technology (NIST, Gaithersburg, MD) was used for statistical analysis of the intima-media thickness measurements.

2.3 Setup

Calibration and Voxelization in Stradx

Calibration is necessary to determine the position and orientation of the U/S scans. Calibration results in three position constants and three calibration constants that are used with the images and corresponding position information during the reconstruction process. Full details of the automatic calibration technique used in the Stradx software are described in [20]. Briefly, to perform the calibration, the components of the Flock of Birds are positioned as described earlier, with the transmitter of the position sensor mounted in a fixed position on the wooden table and the receiver of the position sensor mounted on the U/S transducer. In our experiments a single-wall phantom was used for calibration. Specifically, the calibration was performed by imaging the floor of a glass fish tank filled with water. While continuously capturing the U/S images, the U/S transducer was put through a series of motions described in [20] which fully define the transducer's range of motion.

In the calibration process, we are concerned with four different coordinate systems: the coordinate system of the B-scan plane, the coordinate system of the position sensor's receiver, the coordinate system of the transmitter, and the coordinate system of the reconstruction volume. After a set of 2D U/S images is obtained by sweeping the transducer over the specimen, volume reconstruction is carried out by transforming the pixels of each individual 2D U/S image from the original coordinate system of the B-scan plane, to the coordinate system of the receiver, then to the coordinate system of the transmitter, and finally to the coordinate system of the reconstruction volume. After the pixels of each 2D image are transformed to the coordinate system of the reconstruction volume, intensities are assigned to each voxel of the reconstructed volume based on interpolation of the intensities of neighboring and intersecting pixels. These voxel intensities define the 3D volume used in subsequent processing steps.

2.4 Data Acquisition Procedure

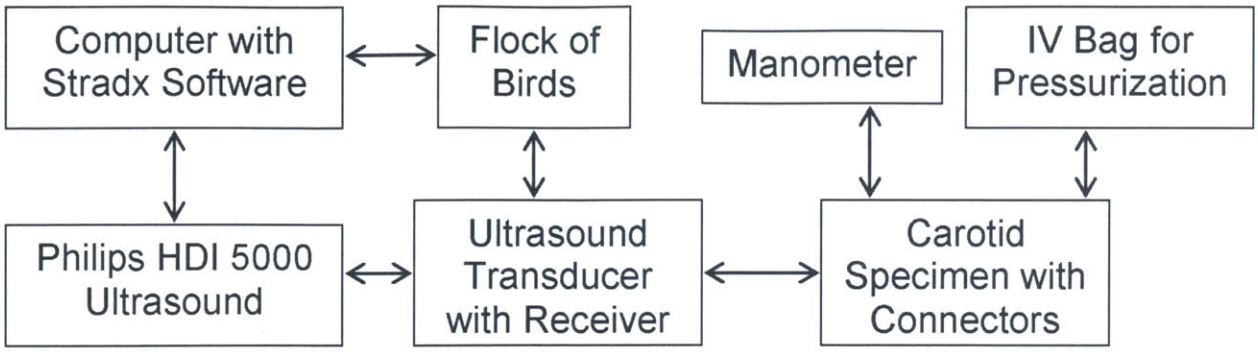

Figure 2-4. Overall flow of information.

Ex-vivo carotid artery specimens were obtained from autopsies performed in the Department of Pathology at Massachusetts General Hospital (Boston, MA). Specimens were stored in phosphate buffered saline (PBS) at 4°C for imaging within 24 hours of harvesting. Before scanning, extraneous connective tissue and fat were removed from the specimens. Appropriately sized plastic tubing connectors from Value Plastics, Inc. (Fort Collins, CO) were inserted into the common, internal, and external branches of the specimen such that the connectors fit snugly into the lumen.

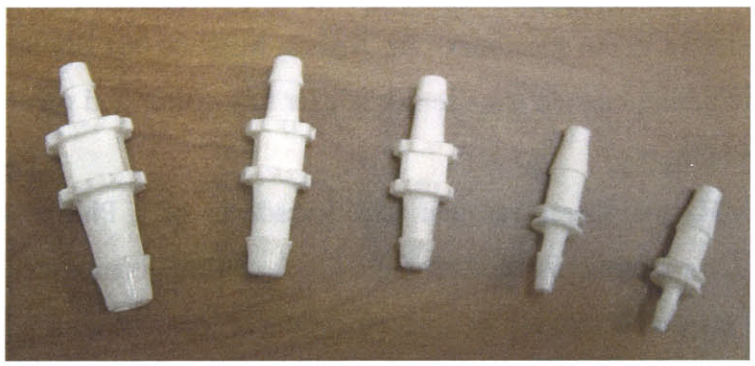

Figure 2-5. Plastic tubing connectors from Value Plastics, Inc.

Medical sutures were circumferentially tied around the connector to securely seal the connector to the artery. Side branches in the specimen were sutured to prevent leakage. The connections were then tested to ensure minimal to no leakage out of the connector and the specimen. After

the connectors were sutured to the specimen, the specimen was mounted in clay holders attached to a Velcro base and arranged so that the specimen was held taut, but was not stretched or loose. One to two inch sections of plastic tubing were then secured to two of the plastic tubing connectors, and the specimen holder containing the specimen was immersed in a shallow saline bath.

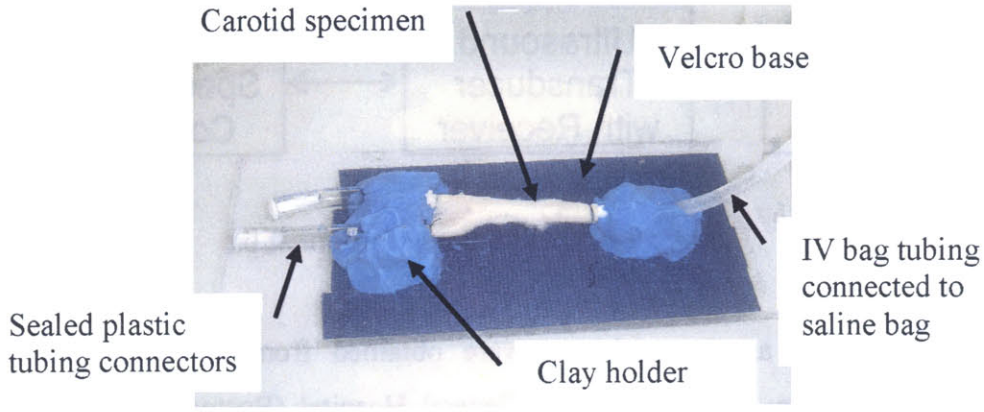

Figure 2-6. Ex-vivo carotid specimen mounted in specimen holder, with plastic tubing attached to plastic tubing connectors secured in the internal, external, and common branches.

Medical IV bag tubing is used to connect the third plastic tubing connector to a saline bag. The specimen is flushed with saline and the two pieces of plastic tubing are sealed off. This allows the specimen to fill with saline (assuming minimal leakage out of the sutured ends has been obtained); it also allows for the pressure inside the specimen to be varied by changing the height of the saline bag relative to the specimen. An Artisan MP2000.001 digital manometer attached to one of the plastic tubing connectors allows the user to monitor and record the internal carotid pressure during scanning.

The 12-5 MHz peripheral vascular U/S transducer of a Philips HDI 5000 Sono CT machine was used for scanning. A receiver for a Flock of Birds is mounted on the transducer so that movements of the transducer can be tracked and recorded through the Flock of Birds by the Stradx software throughout the scan.

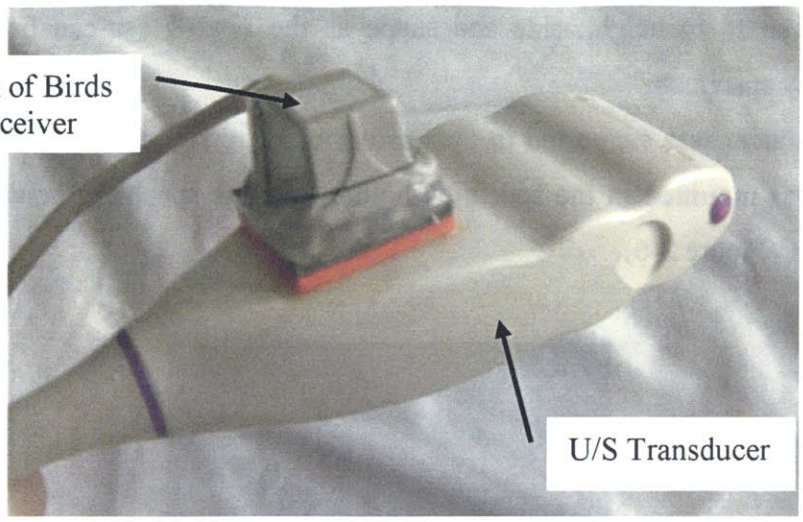

Figure 2-7. U/S transducer with Flock of Birds receiver attached.

The transducer is mounted in a custom built linear translation device made out of Lego® building blocks.

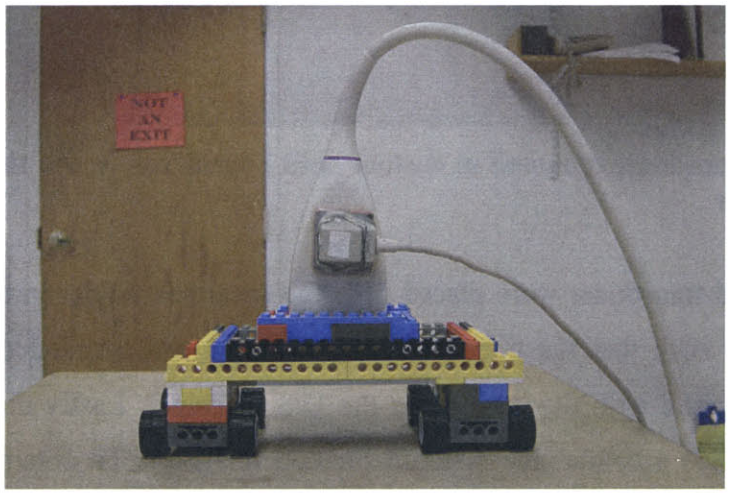

Figure 2-8. U/S transducer with attached Flock of Birds receiver, mounted in custom built linear translation device.

The device allows the user to translate the transducer smoothly, slowly, and evenly over the specimen. It is crucial that movements of the transducer are slow and smooth so that the captured U/S images are not blurry. Also, the somewhat uneven translation of the transducer using the custom built Lego® car was desirable compared to the exact translation that could be obtained using a standard linear motion device, as the inexact translation better simulated the motion that would be seen when scanning a carotid in-vivo. The Lego® car also allows for

flexibility with regard to height, size and shape as the Lego® car can be easily adapted to accommodate any specimen.

The transducer was supported in the custom built Lego® car for scanning (Figure 2-8). The specimen was mounted in the specimen holder, and the specimen holder was placed in a shallow container (Figure 2-6).

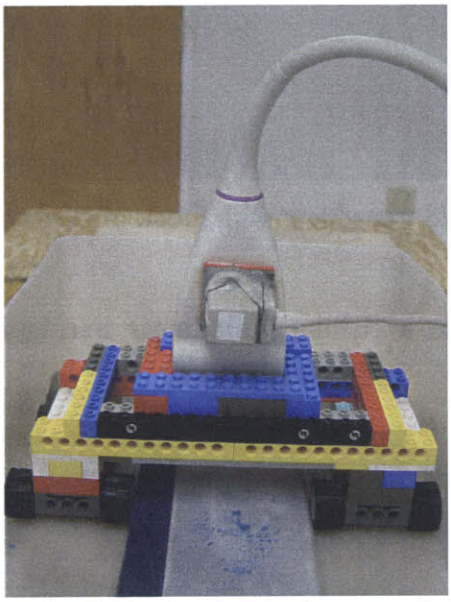

Figure 2-9. U/S transducer mounted in custom built Lego® car, in the shallow container, over the specimen holder.

The Lego® car and transducer were placed over the specimen holder in the shallow container, and were arranged such that the transducer was centered and suspended 2-2.5 cm above the specimen to correspond with the settings on the U/S machine. Lastly the container was filled with saline to provide a conductive medium for U/S imaging. To obtain the U/S images, the transducer was held steady in the Lego® car while the Lego® car was translated slowly over the specimen. As Stradx records the U/S images, it simultaneously records the location of the transducer through the position and orientation measurements obtained from the Flock of Birds. The dense sequence of U/S images recorded, combined with the position information, allows for the creation of 3D U/S volumes within the Stradx software.

Before each specimen was analyzed, the internal carotid pressure was stabilized by adjusting the height of the saline bag while monitoring the pressure on the digital manometer. Pressures in the range of 80-120 mmHg were used, as this range corresponds to an average,

healthy, in-vivo human blood pressure. For each specimen analyzed 5 scans were recorded and voxelized. The 3D volumes created when the files are voxelized are used as input to our fully 3D processing scheme to extract final vessel wall boundaries, from which measurements of intima-media thickness can be made.

Figure 2-10. Overall scanning setup.

Chapter 3

Image Processing

3.1 Background

Segmentation

Segmentation is the process of separating an image into regions. Features in the image, or segmentation techniques are used to classify the type of segmentation. While segmentation is a crucial step in image processing, there are many problems one might run into when implementing different segmentation techniques. Variations in object shape and size between images, and variations in image quality can make a standardized segmentation method difficult to compose. Weak boundaries, noise, poor contrast, and poor spatial resolution can also pose difficulties when segmenting an image. Specifically, noise and sampling artifacts in medical images can pose problems with classical segmentation techniques (which use mainly pixel gray level intensities) such as thresholding and edge detection. Deformable models can be used to combat these complications as they incorporate prior information which can help with discontinuities and weak boundaries obtained with classical segmentation techniques.

Three classical segmentation techniques are region based, edge based, and classification. Region based segmentation techniques use similarities within regions and differences between regions to separate the regions, most commonly through thresholding. With thresholding, pixels can be grouped after comparing each pixels' value to one or multiple threshold values. This technique is very easy to implement, and can be quite effective at separating out the regions of interest in the image. Thresholds can be customized to the image and task at hand by setting global or local thresholds, and by using point based or region based thresholding techniques [21].

Edge based techniques comprise a large subset of the segmentation class of image processing. Edges separate regions in an image based upon distinct characteristics such as texture, gray level, or luminance. Edge detection techniques result in an edge map, which classifies each pixel in the image as an edge or non-edge pixel. When regions are defined by their luminance, edges are defined when there is an abrupt change in pixel value. The requirement that edges be continuous eliminates single extraneous pixels from being classified as an edge, however the extent of continuity is set by the user as it can vary depending on the particular image being analyzed. Techniques for edge detection include the gradient method and the Laplacian method. In the gradient method, edges are defined when the first derivative of the image has a local extremum, versus the Laplacian method, where edges are defined when the second derivative of the image is zero. However, one can run into many problems using these methods for edge detection. Sensitivity to noise is one main problem when these methods are applied to medical images, as the derivative operator acts like a high pass filter. Other issues include the need to discretize the image, (resulting in an approximation to the derivative being used rather than the exact derivative), the appearance of false edges, and the problem of missing edges [22].

Deformable Models

Deformable models are curves (2D) or surfaces (3D) defined within the region of interest that change shape and position when subject to internal and external forces. Internal forces are defined within the curve or surface; these forces keep the model smooth during deformation. In contrast, external forces arise from the image data, and move the model toward a feature of interest in the image. Deformable models are advantageous as they allow you to incorporate prior information about the image into the algorithm. This allows the user to compensate for gaps in the desired edge to be extracted, which gives an added robustness to image noise while allowing the user to dictate the smoothness of the final boundaries through the weighting of the internal forces [23].

There are two types of deformable models, parametric and geometric. Parametric models use solely parametric forms to define curves and surfaces during deformation. With parametric models splitting and merging of parts of the model can be difficult, however the user can directly interact with the model. Geometric models are based on the theory of curve evolution, and use

the level set method to represent curves and surfaces as a level set of a higher-dimensional scalar function. The curves or surfaces are then parametrized after deformation is complete [23].

After being initialized near the edge of interest, the energy minimizing parametric deformable model uses internal and external forces to move the curve or surface towards the shape and location of minimum potential energy. The final curve is determined by the parametrized curve which minimizes the total energy, with total energy defined as the weighted sum of internal and potential energy. In the model, the internal elasticity forces hold the curve together, while the internal bending forces prevent the curve from excessive bending. Thus the complete internal energy term controls the tension and smoothness of the curve. The first order derivative in the internal energy term forces the model to behave like an elastic string, as it discourages stretching. A corresponding weighting term allows the user to control the tension of the model. To balance this behavior, the second order derivative in the internal energy term forces the model to behave like a rigid rod, as it discourages bending of the model. Again, a corresponding weighting term exists, allowing the user to control the rigidity of the model. In contrast, external forces are derived from the image data, and attract the curve or surface toward the desired edges in the image. The external energy is defined over the image region of interest, and is minimized at the edges of interest. A potential form for the external energy term consists of a Gaussian convolved with the image, allowing the user to control the capture range of the deformable surface by varying the standard deviation of the Gaussian [23-24].

3.2 Our Technique

Our approach to segmentation of the carotid vessel wall is a non-linear, variational, energy minimization. After voxelization of the sequence of 2D U/S images into 3D volumes, direction sensitive smoothing is used to extract and enhance the inner (intima-lumen boundary) and outer (media-adventitia boundary) edge fields. A custom designed technique dubbed DEEE is then applied to the outer edge field to eliminate extraneous edges that still remain. A deformable surface is used together with the initial boundary estimates indicated by the user and the enhanced edge fields to extract the final vessel boundaries.

After the sequences of 2D ultrasound images have been collected as previously described, the first step in the processing of these images is transformation into 3D volumes. After image acquisition, Stradx software is used together with the position information recorded by the Flock of Birds to transform the image data represented by pixels in the sequence of 2D images into corresponding voxels, which together create a 3D volume representation of the specimen of interest. Once the 3D volume has been created the volume is resampled into equally spaced, orthogonal slices. At this point, the slices span the full extent scanned by the user. The user can then select the region of interest they would like to analyze within the full volume. Due to memory and time constraints, the user may choose not to analyze every slice in the selected volume, but rather may analyze every nth slice (n=5 in our case), which due to the thinness of the slices (voxels are 0.078802 mm/side), would still thoroughly describe the desired volume. After the slices to be analyzed are designated, the image data is loaded into Matlab, and the user indicates a rough approximation of the inner and outer boundaries of interest on each slice through manual point selection (approximately 8 and 12 points respectively for the intima-lumen and media-adventitia boundaries).

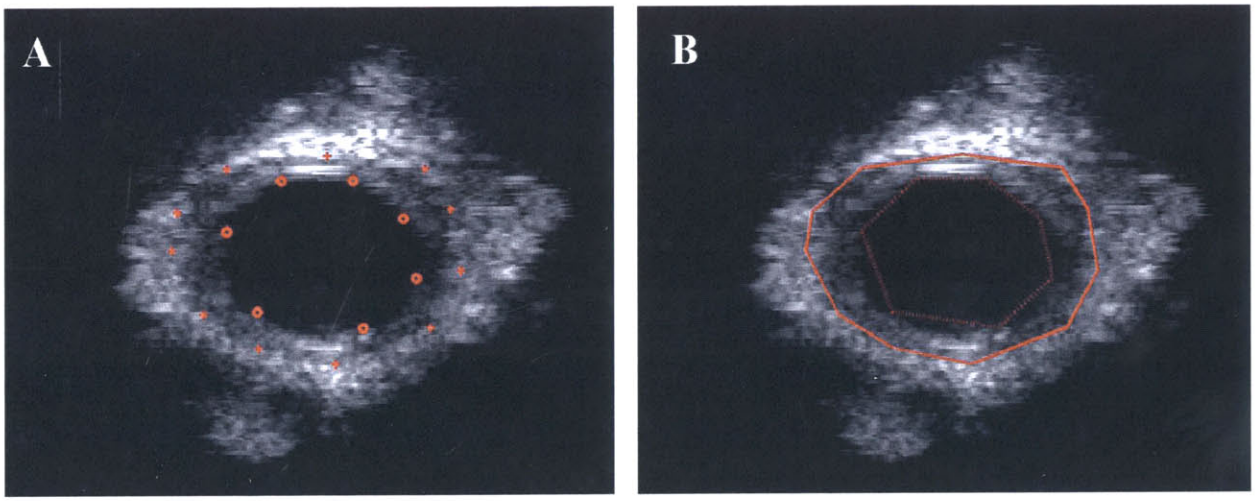

Figure 3-1. Sample cross section of original 3D U/S image volume. 3-1 A. Original points from manual point selection of the inner and outer boundary. 3-1 B. The same cross section with the same points, with the points connected by straight lines.

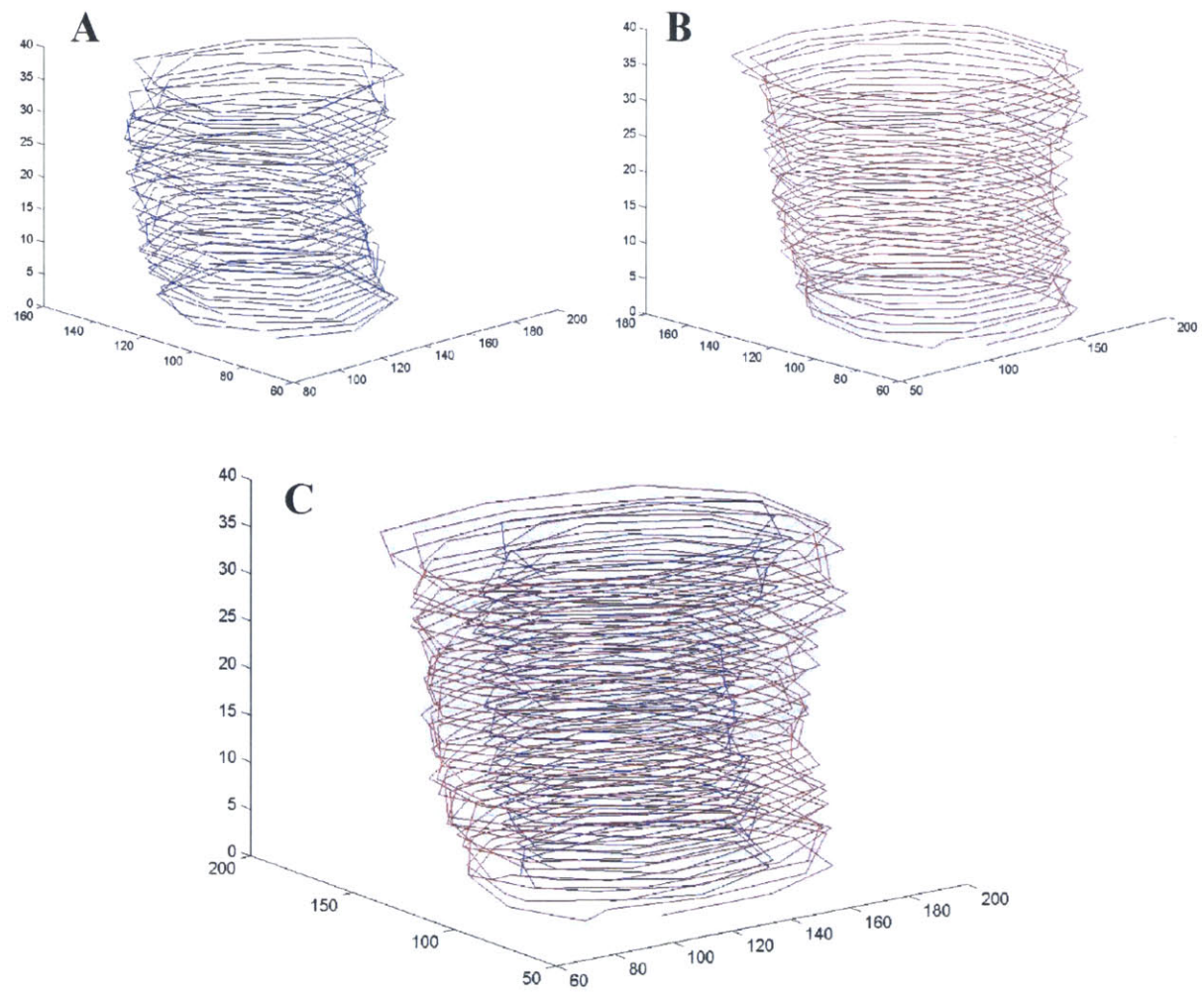

Figure 3-2. Sample input points (connected with straight lines) from manual point selection of one U/S volume. 3-2 A. Points defining the intima-lumen boundary. 3-2 B. Points defining the media-adventitia boundary. 3-2 C. Points defining both boundaries.

Viewed together, the user indicated points on each slice create a rough estimate of the 3D surfaces defining the intima-lumen and media-adventitia boundaries (Figure 3-2). These surfaces provide the starting point for the processing steps applied to the volumes, and allow for fully 3D processing of the images.

The first step in the processing is the warping of the volumes. An averaging filter is used to smooth the rough, user indicated surface along the dimension corresponding to the axial length of the specimen (window size of 8 voxels along the length). The Matlab *surfnorm* command is used to calculate 3D surface normals for each voxel defined along the smoothed surface using a bicubic fit of the data. Using 3D linear interpolation along these surface normals

(interp3), the volume is morphed so that the irregular surface defined by the user is warped into a flat plane. The surface normals for the inner and outer vessel wall surfaces are calculated separately, and the volume is warped twice, once to morph the intima-lumen surface into a plane, and a second time to morph the media-adventitia surface into a plane.

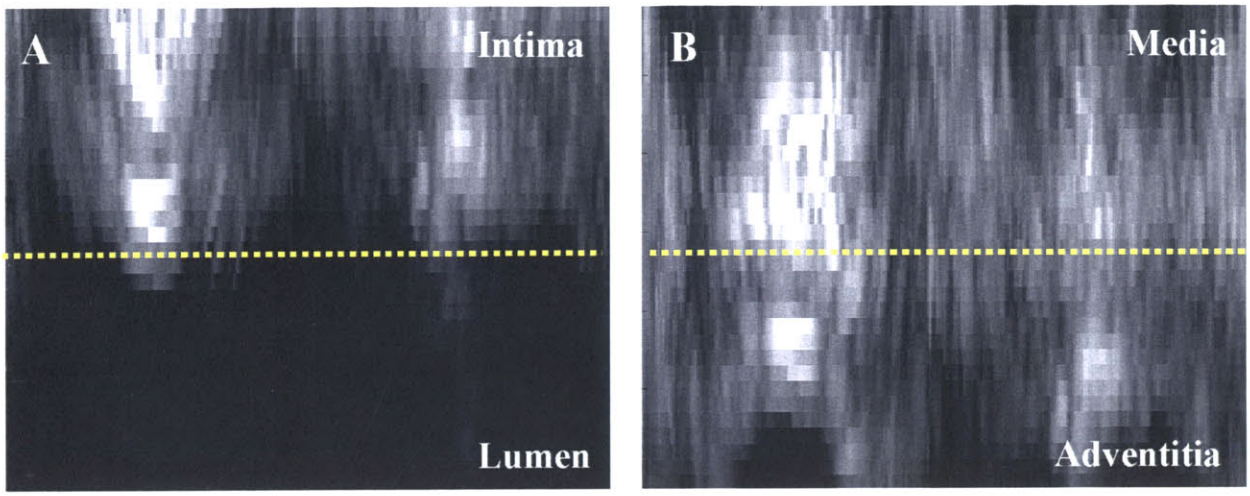

Figure 3-3. Cross sections of 3D warped edge fields before direction sensitive smoothing. Yellow lines indicate the roughly horizontal (planar) boundary. 3-3 A. Warped intima-lumen boundary. 3-3 B. Warped media-adventitia boundary.

For subsequent processing steps, these two morphed volumes are processed separately. At the end of the process when final vessel boundaries are extracted, the intima-lumen and media-adventitia boundaries are put together to fully define the 3D morphology of the carotid vessel wall.

3D anisotropic smoothing and edge enhancement are then performed on the warped volumes using a directionally sensitive energy functional. Our approach uses an adaptation of the Shah unification functional for variational energy segmentation [25].

$$E_{Shah}(f,s) = \iint_R \underbrace{\alpha(1-s)^2 \|\nabla f\|_1}_{\text{Smoothness Constraint}} + \underbrace{\beta\|f-g\|_1}_{\text{Data Fidelity}} + \underbrace{\frac{\rho}{2}\|\nabla s\|_2^2 + \frac{s^2}{2\rho}}_{\text{Edge Penalty}} dxdy \quad (1)$$

The Shah unification functional consists of a smoothness constraint term, a data fidelity term, and an edge penalty term. The smoothness constraint term penalizes large gradients in the

anisotropically smoothed field, f, except where edges exist. Values for the edge field, s, range from 0 to 1, with 1 representing an edge. The data fidelity term controls the degree to which the smoothed field f resembles the original image data, g. Lastly, the edge penalty term controls the edge width and prevents the minimization process from placing edges everywhere in the edge field. Coupled with each term is a weighting parameter, which can be varied to control the degree to which each term contributes to the overall energy equation.

The Shah unification functional Equation 1 is advantageous as it makes use of L1 norms rather than L2 norms. The use of L1 norms permits the development of intensity discontinuities at structure boundaries that the L2 norm inherently prevents, as it oversmooths solutions. Also, the Shah energy functional provides a common framework for curve evolution, segmentation, and anisotropic diffusion. The Shah unification functional allows the level curves of the smoothed image and the edge field to evolve simultaneously until they converge, with each impacting the other throughout the process. This eliminates the need to extract an initial edge field earlier in the process through a means such as linear filtering.

Adaptation of the Shah unification functional in 3D, seen below, incorporates directional sensitivity to the weighting parameter for the gradient term and was used here for processing [26].

$$E_{DS}(f,s) = \int_V \underbrace{(1-s)^2\{D(f)\}}_{\text{Smoothness Constraint}} + \underbrace{\beta\|f-g\|_1}_{\text{Data Fidelity}} + \underbrace{\frac{\rho}{2}\|\nabla s\|_2^2 + \frac{s^2}{2\rho}}_{\text{Edge Penalty}} dV \qquad (2)$$

$$D(f) = \alpha_x \left\| \frac{\partial f}{\partial x} \right\|_1 + \alpha_y \left\| \frac{\partial f}{\partial y} \right\|_1 + \alpha_z \left\| \frac{\partial f}{\partial z} \right\|_1$$

Since our ultrasound volumes have been warped such that the desired surfaces are roughly planar, we can enhance or eliminate edges based on their orientation in the warped volume using the α_x , α_y , and α_z weighting parameters. Vertically aligned edges can be safely eliminated, while horizontally aligned edges should be enhanced. Incorporating this extra information

allows for elimination of edges which are strong yet are likely false edges due to their vertical orientation, and enhancement of edges which are weak yet are likely true edges due to their horizontal orientation. Since warping of the volumes is done based on rough initial point selection by the user, the true edges in the warped volume may not be perfectly planar. Thus the weighting parameters added to the gradient terms are implemented independently (α_x , α_y , and α_z versus just one α term), allowing the user to control the relative weighting of the edges based on their direction. This is in contrast to distinguishing between edges based on their exact orientation perpendicular or parallel to the desired orientation, resulting in full elimination or enhancement of each edge considered. Empirically determined parameters of $\alpha_x = 10$, $\alpha_y = 30$, $\alpha_z = 50$, $\beta = 0.03$, and $\rho = 0.002$ were used to process the intima-lumen boundary, and parameters of $\alpha_x = 50$, $\alpha_y = 100$, $\alpha_z = 100$, $\beta = 0.03$, and $\rho = 0.001$ were used to process the media-adventitia boundary.

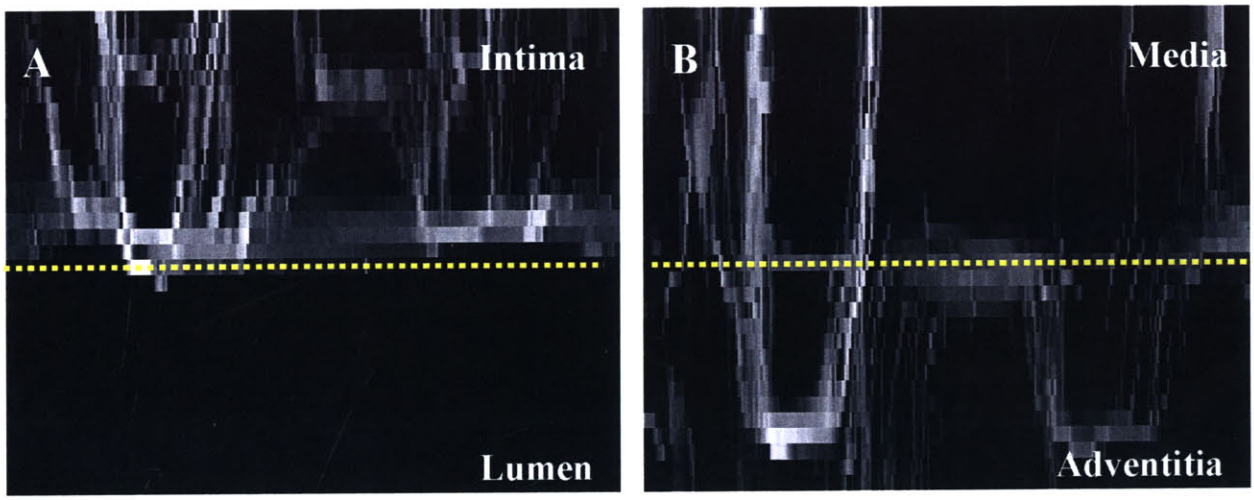

Figure 3-4. Warped edge fields after direction sensitive smoothing. Yellow lines indicate the roughly horizontal (planar) boundary. 3-4 A. Warped intima-lumen boundary. 3-4 B. Warped media-adventitia boundary.

Numerical solution of Equation 2 is performed using iterative minimization of the discretized energy functional with a coordinate descent approach [26]. The coordinate descent approach involves dividing Equation 2 into two simpler energy terms [27]. By alternately fixing the edge field s and minimizing with respect to the smoothed field f, and fixing the smoothed field f and minimizing with respect to the edge field s, the joint minimizer of the two equations

and thus the minimization of the overall equation can be determined. A pre-conditioned conjugate gradient algorithm is used for each of the minimizations. The conjugate gradient algorithm is advantageous as it converges rapidly if appropriate preconditioners are chosen [28]. Our implementation uses an initialization of f = g and s = 0, and iterates until a specified convergence is reached [27].

The directionally sensitive smoothing technique alone is sufficient to extract the 3D edge fields corresponding to the intima-lumen surface because of the distinct boundary distinguishing this surface in the U/S image. However, an extra processing step is necessary to extract a clear 3D edge field corresponding to the media-adventitia boundary. After applying the initial directionally sensitive smoothing and edge enhancement technique to the warped volume corresponding to the outer vessel surface, a custom designed filtering technique we've dubbed 'DEEE' is applied. DEEE is a technique to eliminate extraneous false edges in the enhanced edge field produced in the previously described processing steps that may have slipped through the directionally sensitive edge enhancing energy minimization. This process serves to eliminate small, isolated groups of high intensity voxels based on the principle of continuity of edges. It is assumed that true edges are continuous – in the warped view of the volumes, continuity of edges should exist horizontally along cross-sections of the volume, and along the depth of the warped volume. Thus if a high intensity voxel exists in an area where it is surrounded horizontally and depth-wise by other high-intensity voxels, then the voxel is assumed to be part of a true edge, as the test of edge continuity holds. If a high intensity voxel is isolated, or exists only in a small group within the volume, this voxel or group of voxels is assumed to be an extraneous (false) edge that can safely be eliminated, as it does not pass the test of edge continuity.

DEEE uses a threshold intensity value set for each volume according to a lower truncation of the mean intensity of all voxels comprising the volume. The program first checks each voxel of the volume, comparing it's intensity to the threshold intensity value. If the voxel value is less than the threshold intensity, the voxel value is reset to 0 (black). For voxels above the threshold intensity, the program checks neighboring voxels to determine the likelihood that the voxel of interest is part of a true edge.

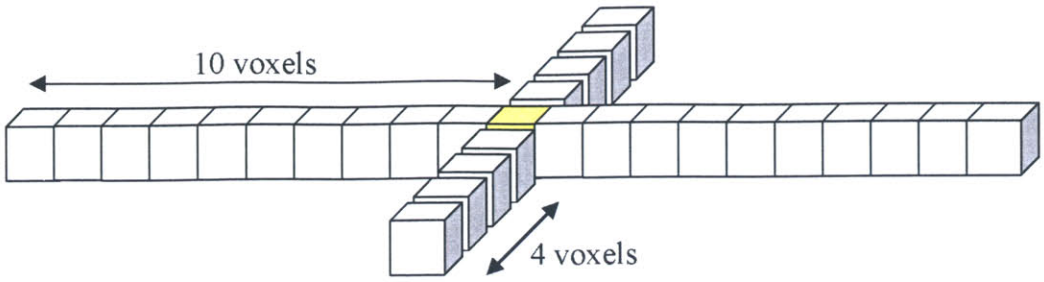

Figure 3-5. Range of voxels analyzed in DEEE. The center voxel (yellow) is the voxel of interest.

The likelihood of the voxel being a part of a true edge is determined by analyzing 10 voxels to the right and 10 voxels to the left of the voxel of interest (as the true edges should be roughly horizontally aligned in the warped image). Voxels in neighboring slices (4 voxels behind and 4 voxels in front of the voxel of interest) with the same coordinates are also analyzed. If it is found that greater than 8 voxels within this localized volume of voxels surrounding the voxel of interest are below the threshold voxel intensity value, it is assumed that the voxel of interest is an extraneous voxel, and is not part of a true edge and the voxel of interest is set to intensity = 0. If less than 8 voxels within the localized volume of voxels being analyzed have intensity levels below the threshold intensity value, then the voxel of interest is assumed to have a high likelihood of belonging to a true edge. In this case, the voxel maintains it's original intensity value.

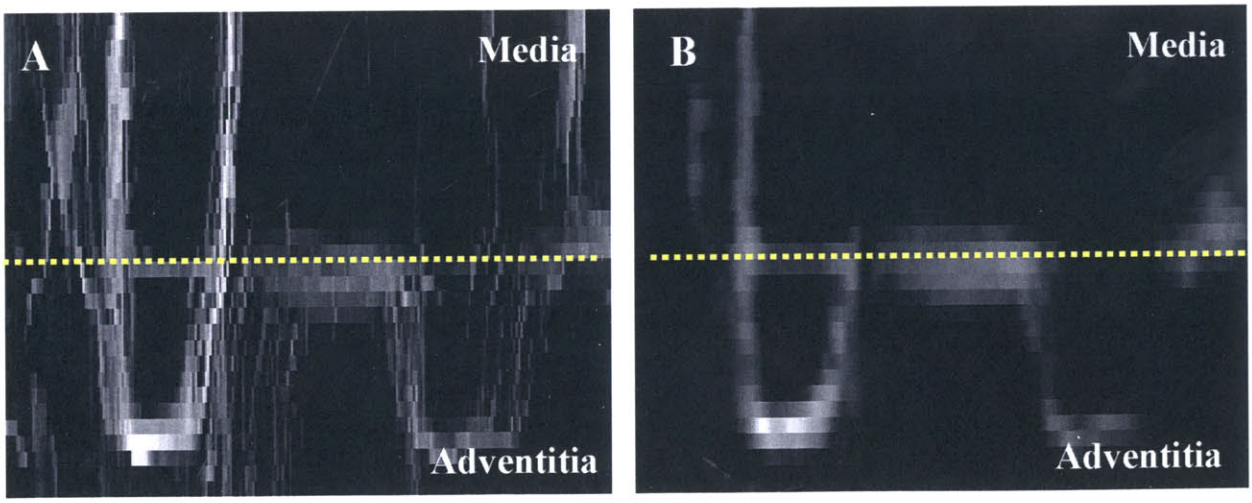

Figure 3-6. Warped media-adventitia boundary before and after DEEE. Yellow lines indicate the roughly horizontal (planar) boundary. 3-6 A. After direction sensitive smoothing, but before DEEE. 3-6 B. After direction sensitive smoothing and after DEEE.

After obtaining a cleaner edge field with fewer false edges, the edge field is warped back into the coordinate state of the original volume using the reverse of the transformations from the initial warping. This enhanced edge field is then used together with initial surface locations indicated by the user to evolve deformable surfaces to the inner and outer vessel boundaries. The deformable surfaces move over the domain of the U/S volume to minimize the energy functional shown below, where the external energy term consists of a 3D Gaussian convolved with the enhanced 3D edge field to control the capture range of the deformable surface X.

$$E_{deform}(x) = \int_{t_1}\int_{t_2} \frac{1}{2} a \left\{ \left\| \frac{\partial x}{\partial t_1} \right\|_2^2 + \left\| \frac{\partial x}{\partial t_2} \right\|_2^2 \right\} + \frac{1}{2} b \left\{ \left\| \frac{\partial^2 x}{\partial t_1^2} \right\|_2^2 + \left\| \frac{\partial^2 x}{\partial t_2^2} \right\|_2^2 + \left\| \frac{\partial^2 x}{\partial t_1 \partial t_2} \right\|_2^2 \right\} - E_{ext}(x) dt_1 dt_2 \quad (3)$$

$$E_{ext}(x, y) = G_\sigma(x, y, z) * s(x, y, z)$$

The enhanced edge field serves to pull points on the deformable surface towards areas of maximum boundary gradients, while the deformable surface simultaneously adapts its shape to minimize the energy associated with surface stretching and bending. Empirically determined parameters of a = 0.0006 and b = 0.0006 were used to process the intima-lumen boundary, while parameters of a = 0.01 and b = 0.02 were used to process the media-adventitia boundary. The deformable surface is applied to the 3D enhanced edge field corresponding to the intima-lumen boundary, and also to the 3D edge field corresponding to the media-adventitia boundary. The final result of applying the deformable surface to these two edge fields is an output of two sets of points describing the 3D surfaces corresponding to the intima-lumen and media-adventitia boundaries on the specimen.

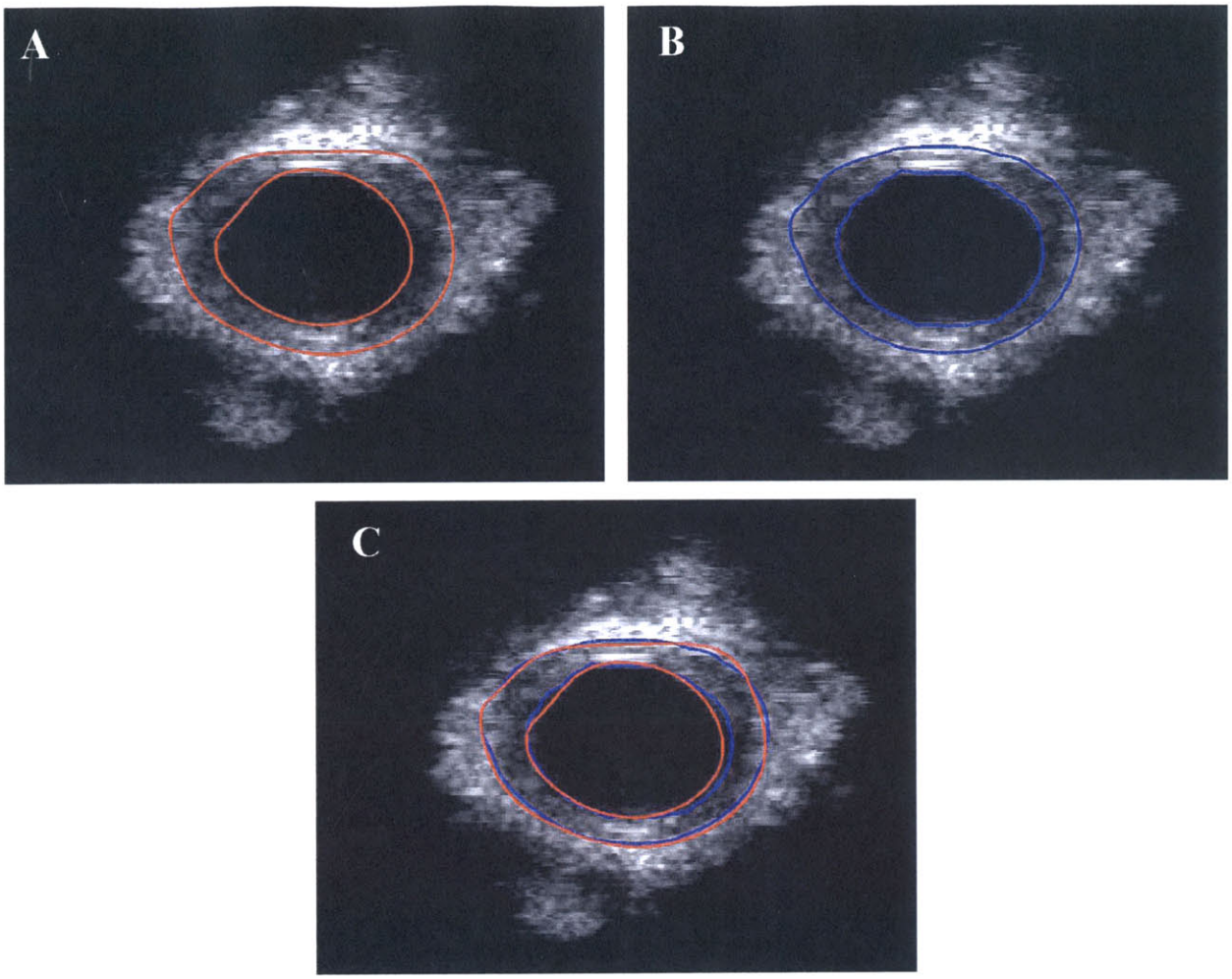

Figure 3-7. Sample cross section of 3D U/S image volume. 3-7 A. Inner and outer boundaries as indicated in the manual point selection. 3-7 B. Final inner and outer boundary points determined from our fully 3D automatic technique. 3-7 C. Both boundaries – manual point selection in red, automatic point selection in blue.

After these final boundaries are determined, they can be used to calculate the intima-media thickness for the specimen of interest. The intima-media thickness is computed by calculating the Euclidean distance between the inner and outer boundaries at intervals of 1.44 degrees spanning the full circumference of the vessel wall for each slice in the volume. Using these 250 values, an average IMT is calculated for each slice.

Chapter 4

Results and Discussion

4.1 Statistical Analysis Techniques

The calculated differences in IMT between scans were tested for normality using the Anderson-Darling goodness of fit test. The one-sided Anderson-Darling test is a modification of the Kolmogorov-Smirnov test, however the Anderson-Darling test gives more weight to the tails of the distribution than the Kolmogorov-Smirnov test does. Also, the Kolmogorov-Smirnov test does not take into account the specific distribution being tested (in our case normal), while the Anderson-Darling test does. Taking into account the specific distribution being tested allows for a more sensitive test, and while critical values must be calculated for each different distribution, most statistical analysis programs have critical values for common distributions (including normal) built in, so this does not complicate the process. The Anderson-Darling test statistic A^2 is calculated according to [29]. The statistic is then multiplied by a constant to adjust for the sample size, resulting in the adjusted A^2 test statistic. This adjusted test statistic is compared against the critical values to, in our case, test for normality. If the test statistic is greater than the critical value, the null hypothesis that the data have a normal distribution is rejected [29].

The statistical f-test, which assumes normality of the data set, provides a way to test for equality of the standard deviations of two sets of data. The F statistic, a ratio of sample variances, is calculated as follows: $F = \frac{s_1^2}{s_2^2}$, where s_1^2 and s_2^2 are the sample variances. The two-tailed F-test tests against the alternative hypothesis that the two standard deviations are not equal.

The more the F statistic deviates from 1, the stronger the evidence for unequal data set variances [30].

Bland-Altman plots were also used to compare the manual and automatic IMT results. This graphical test is used to assess the degree of agreement between two techniques when no true quantity exists to compare the results to. That is, when indirect methods are used to obtain a result, one must compare the results to an alternative technique rather than a true result. With a Bland-Altman plot, the difference between the results from two methods is plotted versus the mean result of the two methods; because a true result is not known, the mean result of the two methods is the best estimate we have to compare against. This analysis technique assumes that the differences (or the measurement error) are normally distributed, though the raw data is not required to be normally distributed [31].

4.2 Results

Using the processing techniques and parameter values described in chapter 3, section 3.2, IMT measurements were calculated for each U/S volume analyzed. In the results presented, manual IMT measurements refer to IMT measurements calculated from the boundaries defined by the initial point selection from the user. Automatic IMT measurements refer to IMT measurements calculated from the boundaries extracted using our fully 3D processing scheme. It should also be noted that observer 1 was considered an "experienced" observer, as they had basic training in recognizing the carotid vessel wall boundaries on the U/S images. Observer 2 was considered an "inexperienced" observer, as they were shown only a few examples of how to recognize the carotid vessel wall boundaries before they performed their point selection.

For each analysis, the difference in IMT measurements between different point selections was used as input to the statistical tests performed. To calculate the IMT difference for intra-observer tests, the boundaries extracted from each point selection performed by the observer were compared to the mean of the boundaries extracted from other point selections performed by that observer. The results of comparing the boundaries extracted from each point selection to the mean of the boundaries (or each "Test") are shown below. For inter-observer tests, the boundaries extracted from point selections from each observer were compared to the boundaries extracted from point selections of identical volumes from a second observer. The manual and

automatic IMT differences of each test were tested for normality using an Anderson-Darling normality test. The F-test for equivalence of the variances was used to determine if the variances of the manual and the automatic IMT differences for each analysis were statistically equivalent. Lastly, Bland-Altman plots show the difference in IMT measurements between different point selections, as well as allowing one to visualize the difference in the standard deviations (shown in the plots as the 95% confidence interval, or 2* standard deviation) between the manual and automatic data sets.

For intra-observer results, two observers each evaluated one U/S volume (Observer 1, Same Scan 1 and Observer 2, Same Scan 1), performing five separate point selections on the one volume. The intima-media thickness measurements resulting from each point selection were calculated, and were compared frame by frame for each observer (Figures 4-1 and 4-3). This process was repeated by each observer for a second U/S volume (Observer 1, Same Scan 2; Figure 4-2). By repeating the point selection on a single U/S volume, we can see the error in extracting vessel boundaries that is a result of our processing scheme, without introducing error arising from performing multiple scans of the same specimen.

Next, two observers each evaluated five different U/S scans of the same specimen (Observer 1, Multiple Scans and Observer 2, Multiple Scans; Figures 4-4 and 4-5). Before point selection, each of the five scans were cropped such that each U/S volume being analyzed contained the same portion of the specimen. Comparing multiple scans of the same specimen allows us to evaluate the error associated with performing different scans of the same specimen, as well as the error associated with our processing technique.

Data sets were also analyzed to compare automatic and manual IMT results from different observers (Inter-observer, Multiple Scans; Figure 4-6). Five scans of the same specimen were analyzed by both the inexperienced and the experienced observer, and the automatic and manual IMT results obtained by each were compared.

Following we see Bland-Altman plots for each of these data sets, as well as the results of the Anderson-Darling and F-tests.

Intra-Observer: Observer 1 (Experienced), Same Scan 1

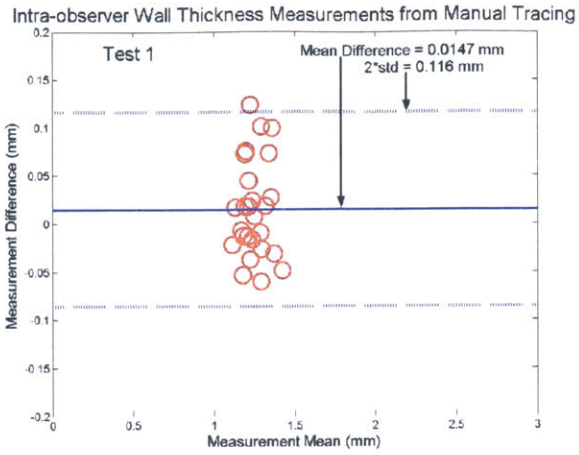

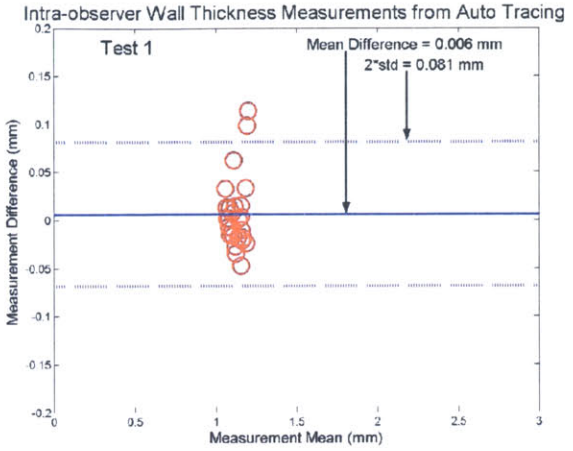

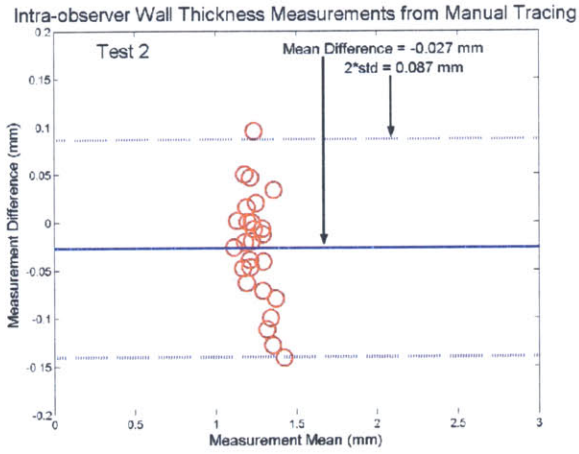

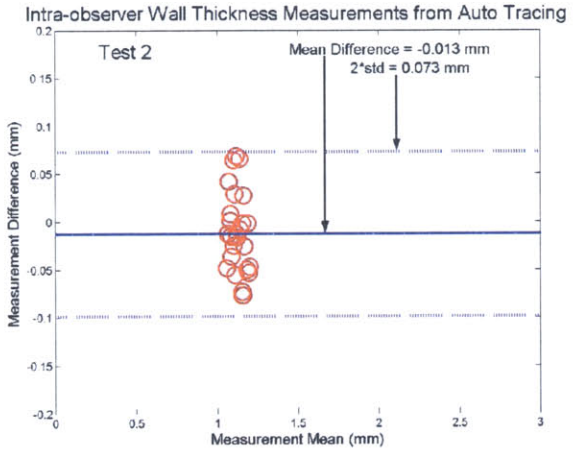

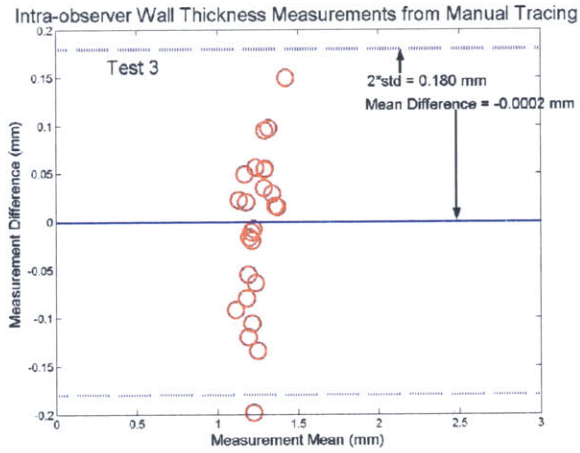

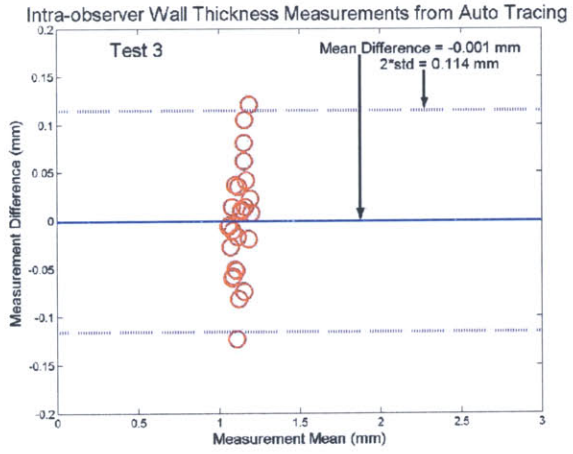

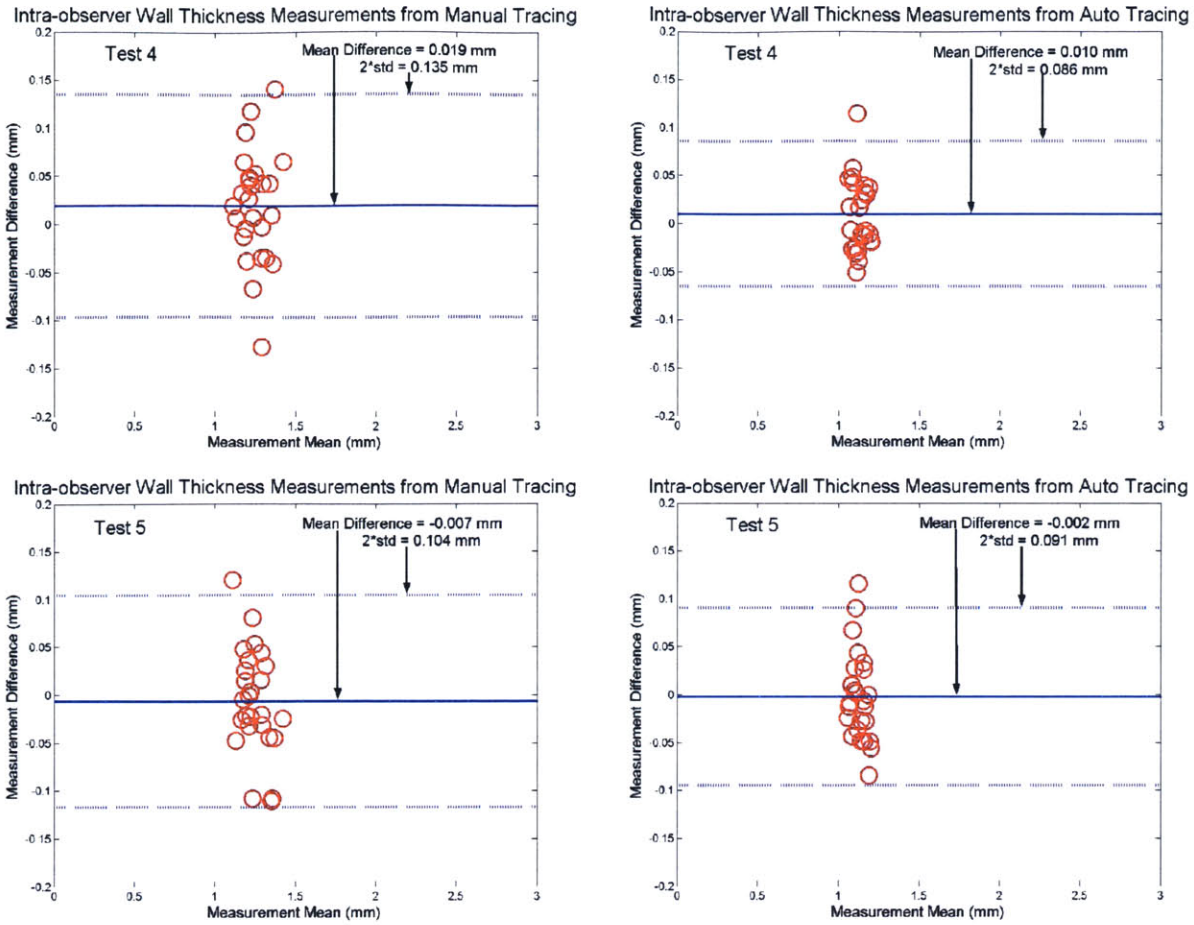

Figure 4-1. Intra-observer results. Bland-Altman plots of intima-media thickness, observer 1, same scan 1. 4-1 A. Manual point selection to determine IMT. 4-1 B. Automatic boundary extraction to determine IMT.

BLAND-ALTMAN				
		Mean IMT (mm)	*Mean IMT Difference (mm)*	*95% Confidence Interval (mm)*
Test 1	***Manual***	1.262	0.0147	0.116
	Auto	1.131	0.006	0.081
Test 2	***Manual***	1.220	-0.027	0.087
	Auto	1.112	-0.013	0.073
Test 3	***Manual***	1.247	-0.0002	0.180
	Auto	1.124	-0.001	0.114
Test 4	***Manual***	1.266	0.019	0.135
	Auto	1.135	0.010	0.086
Test 5	***Manual***	1.241	-0.007	0.104
	Auto	1.123	-0.002	0.091

ANDERSON-DARLING TEST				
		Adjusted A^2 test statistic	*Critical value at 95% confidence*	*Null Hypothesis: Accept or Reject*
Test 1	***Manual***	0.596	0.735	Accept
	Auto	1.432	0.735	Reject
Test 2	***Manual***	0.216	0.735	Accept
	Auto	0.416	0.735	Accept
Test 3	***Manual***	0.282	0.735	Accept
	Auto	0.217	0.735	Accept
Test 4	***Manual***	0.280	0.735	Accept
	Auto	0.623	0.735	Accept
Test 5	***Manual***	0.380	0.735	Accept
	Auto	0.442	0.735	Accept

F-TEST			
	F-test statistic	*F-test statistic CDF value*	*Null Hypothesis: Accept or Reject*
Test 1	1.813	0.928	Reject with 90% Confidence
Test 2	1.747	0.915	Reject with 90% Confidence
Test 3	2.442	0.985	Reject with 95% Confidence
Test 4	2.330	0.980	Reject with 95% Confidence
Test 5	1.425	0.809	Reject with 80% Confidence

Table 4-1. Observer 1, same scan 1. Intra-observer results for Bland-Altman plots, Anderson-Darling normality test and F-test for equivalence of variances.

Intra-Observer: Observer 1 (Experienced), Same Scan 2

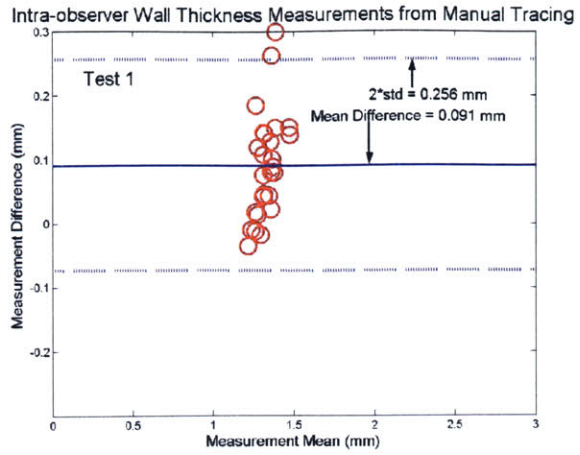

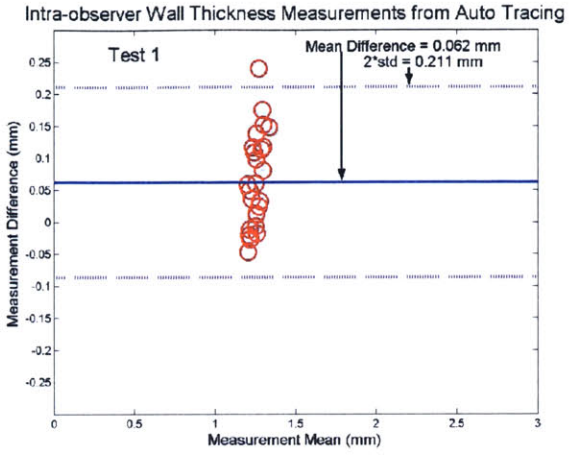

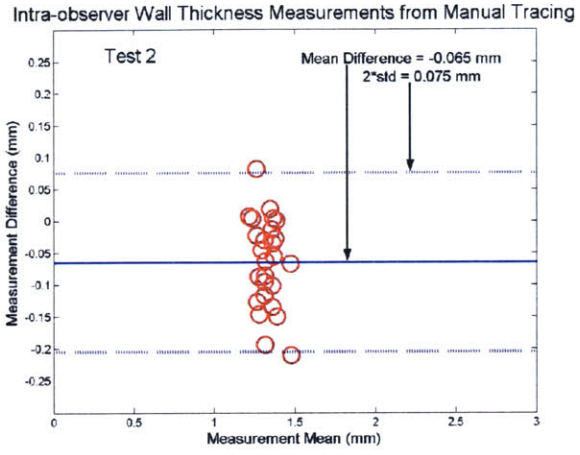

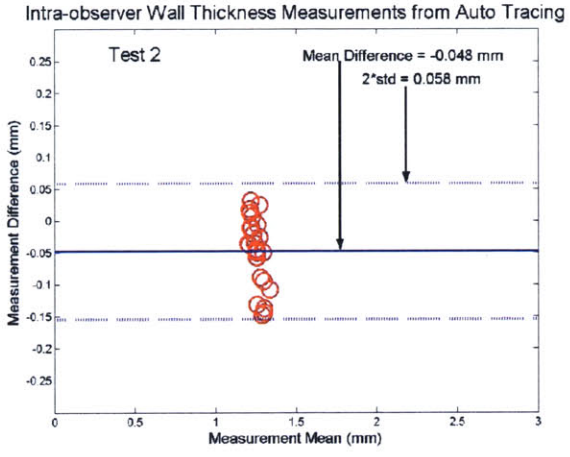

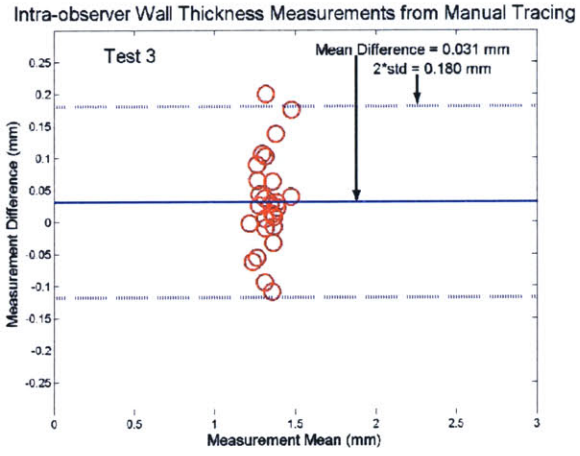

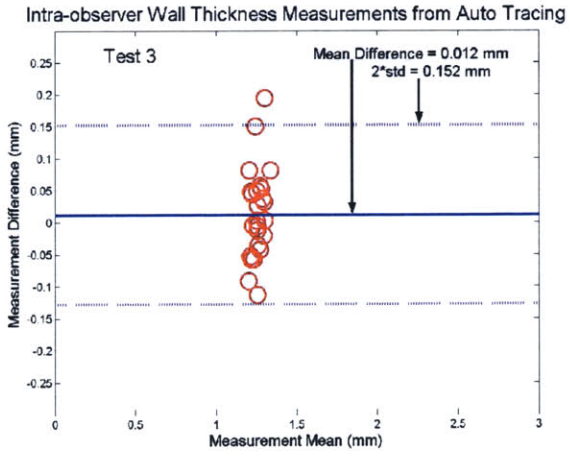

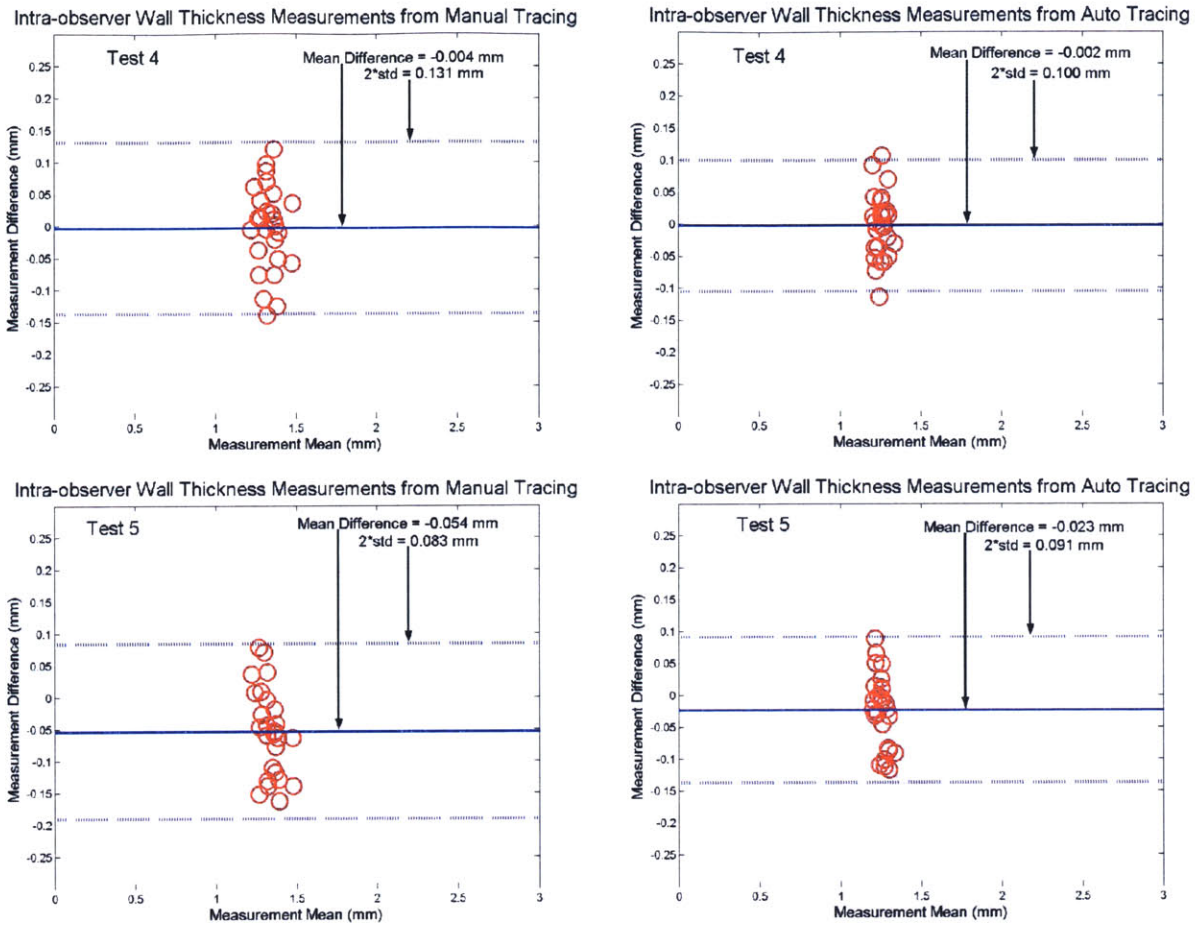

Figure 4-2. Intra-observer results. Bland-Altman plots of intima-media thickness, observer 1, same scan 2. 4-2 A. Manual point selection to determine IMT. 4-2 B. Automatic boundary extraction to determine IMT.

BLAND-ALTMAN				
		Mean IMT (mm)	*Mean IMT Difference (mm)*	*95% Confidence Interval (mm)*
Test 1	***Manual***	1.422	0.091	0.256
	Auto	1.314	0.062	0.211
Test 2	***Manual***	1.266	-0.065	0.075
	Auto	1.203	-0.048	0.058
Test 3	***Manual***	1.362	0.031	0.180
	Auto	1.263	0.012	0.152
Test 4	***Manual***	1.327	-0.004	0.131
	Auto	1.249	-0.002	0.100
Test 5	***Manual***	1.277	-0.054	0.083
	Auto	1.228	-0.023	0.091

ANDERSON-DARLING TEST				
		Adjusted A^2 test statistic	*Critical value at 95% confidence*	*Null Hypothesis: Accept or Reject*
Test 1	***Manual***	0.395	0.735	Accept
	Auto	0.434	0.735	Accept
Test 2	***Manual***	0.241	0.735	Accept
	Auto	0.606	0.735	Accept
Test 3	***Manual***	0.352	0.735	Accept
	Auto	0.368	0.735	Accept
Test 4	***Manual***	0.260	0.735	Accept
	Auto	0.228	0.735	Accept
Test 5	***Manual***	0.362	0.735	Accept
	Auto	0.468	0.735	Accept

F-TEST			
	F-test statistic	*F-test statistic CDF value*	*Null Hypothesis: Accept or Reject*
Test 1	1.238	0.702	Reject with 70% Confidence
Test 2	1.731	0.912	Reject with 90% Confidence
Test 3	1.135	0.623	Reject with 60% Confidence
Test 4	1.724	0.910	Reject with 90% Confidence
Test 5	1.445	0.818	Reject with 80% Confidence

Table 4-2. Observer 1, same scan 2. Intra-observer results for Bland-Altman plots, Anderson-Darling normality test and F-test for equivalence of variances.

Intra-Observer: Observer 2 (Inexperienced), Same Scan 1

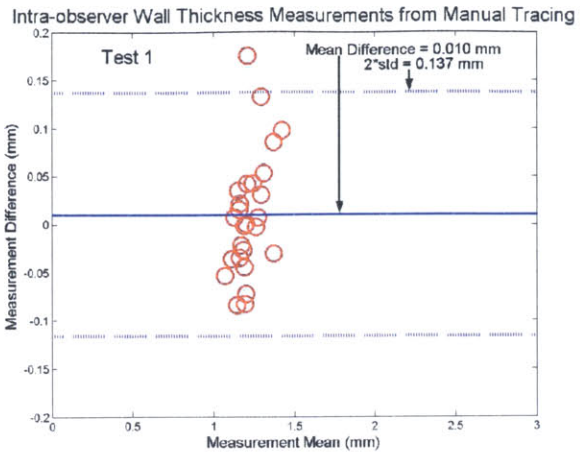

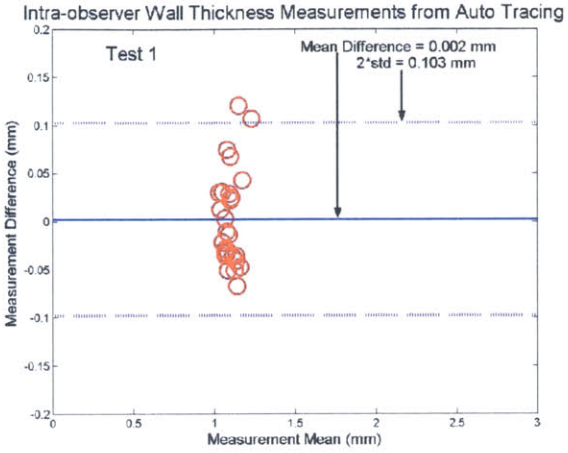

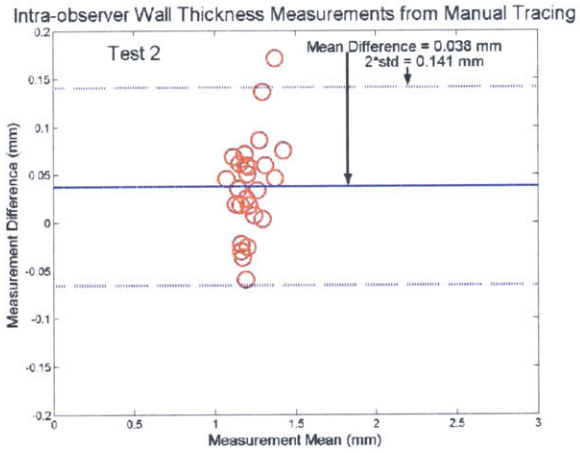

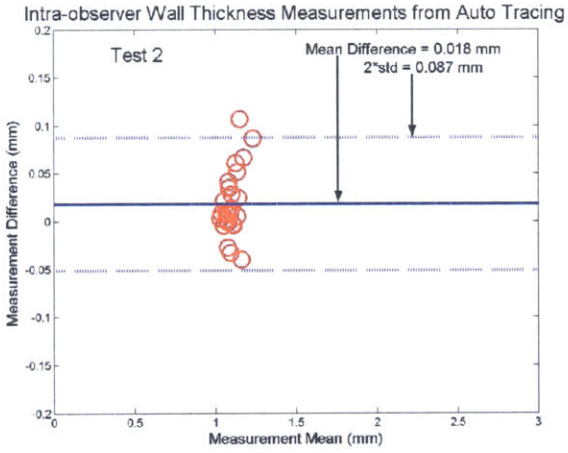

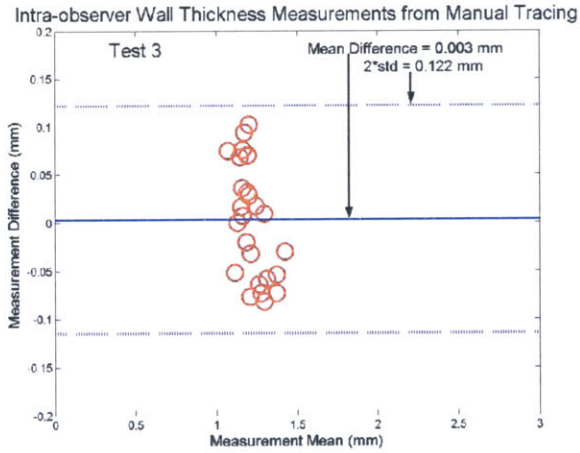

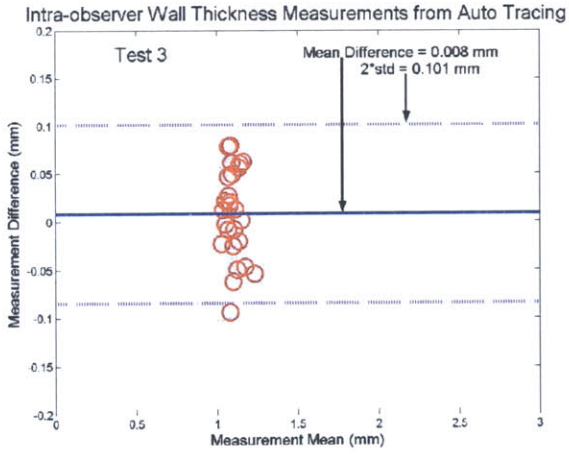

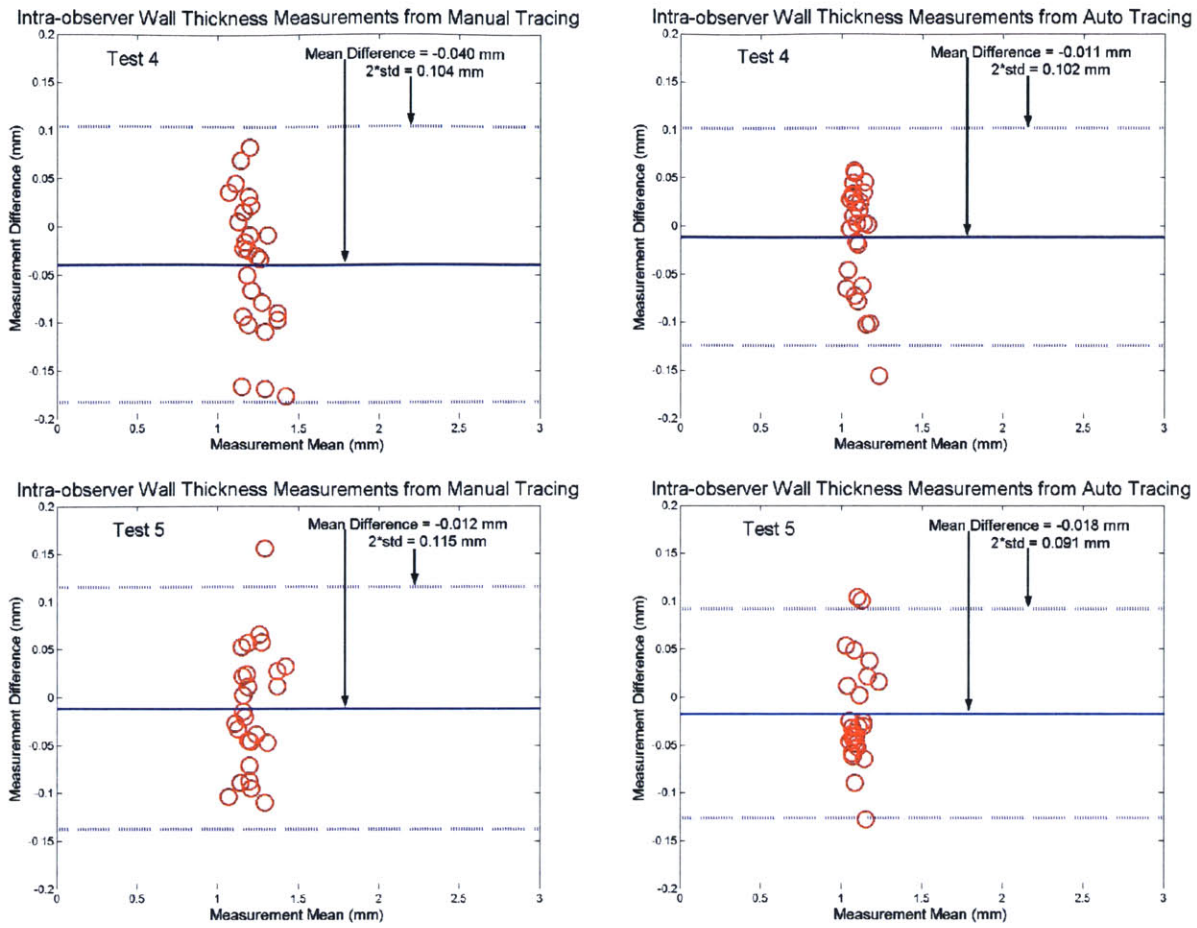

Figure 4-3. Intra-observer results. Bland-Altman plots of intima-media thickness, observer 2, same scan 1. 4-3 A. Manual point selection to determine IMT. 4-3 B. Automatic boundary extraction to determine IMT.

BLAND-ALTMAN				
		Mean IMT (mm)	*Mean IMT Difference (mm)*	*95% Confidence Interval (mm)*
Test 1	***Manual***	1.227	0.010	0.137
	Auto	1.102	0.002	0.103
Test 2	***Manual***	1.255	0.038	0.141
	Auto	1.117	0.018	0.087
Test 3	***Manual***	1.220	0.003	0.122
	Auto	1.108	0.008	0.101
Test 4	***Manual***	1.177	-0.040	0.104
	Auto	1.088	-0.011	0.102
Test 5	***Manual***	1.205	-0.012	0.115
	Auto	1.082	-0.018	0.091

ANDERSON-DARLING TEST				
		Adjusted A^2 test statistic	*Critical value at 95% confidence*	*Null Hypothesis: Accept or Reject*
Test 1	***Manual***	0.409	0.735	Accept
	Auto	0.834	0.735	Reject
Test 2	***Manual***	0.414	0.735	Accept
	Auto	0.872	0.735	Reject
Test 3	***Manual***	0.628	0.735	Accept
	Auto	0.288	0.735	Accept
Test 4	***Manual***	0.308	0.735	Accept
	Auto	1.001	0.735	Reject
Test 5	***Manual***	0.296	0.735	Accept
	Auto	0.854	0.735	Reject

F-TEST			
	F-test statistic	*F-test statistic CDF value*	*Null Hypothesis: Accept or Reject*
Test 1	1.593	0.874	Reject with 85% Confidence
Test 2	2.204	0.973	Reject with 95% Confidence
Test 3	1.616	0.882	Reject with 85% Confidence
Test 4	1.599	0.876	Reject with 85% Confidence
Test 5	1.349	0.770	Reject with 75% Confidence

Table 4-3. Observer 2, same scan 1. Intra-observer results for Bland-Altman plots, Anderson-Darling normality test and F-test for equivalence of variances.

Intra-Observer: Observer 1 (Experienced), Multiple Scans

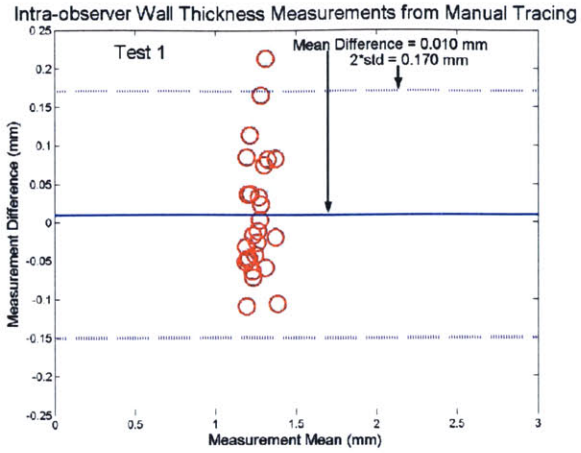

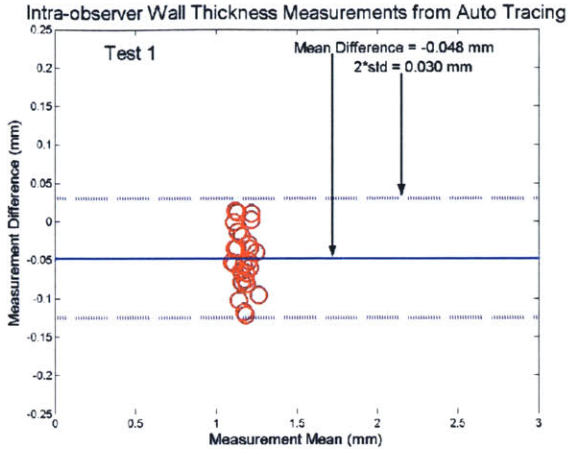

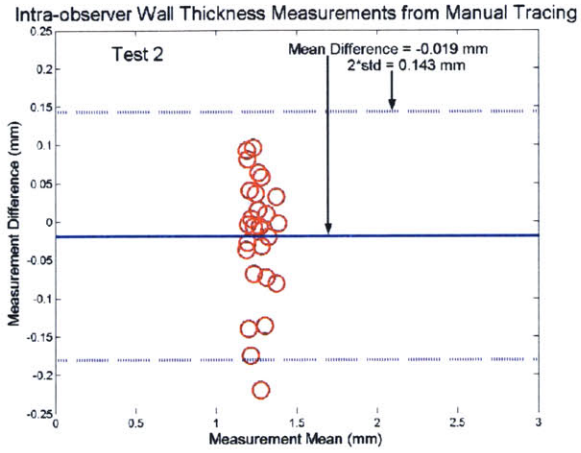

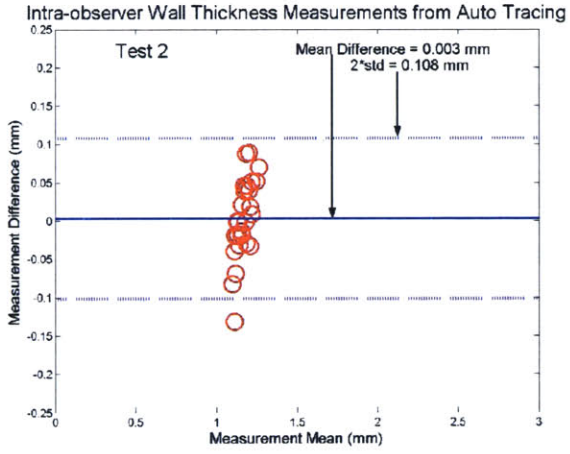

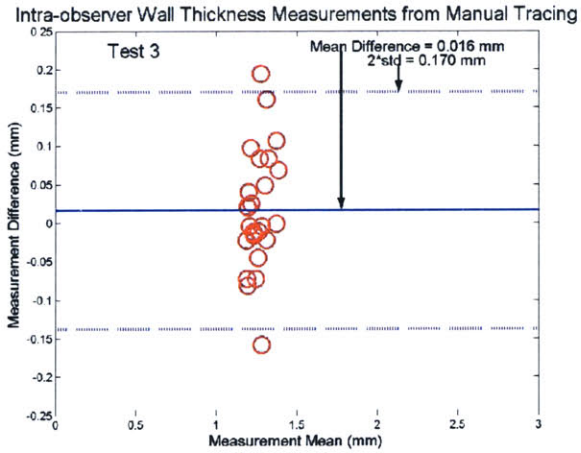

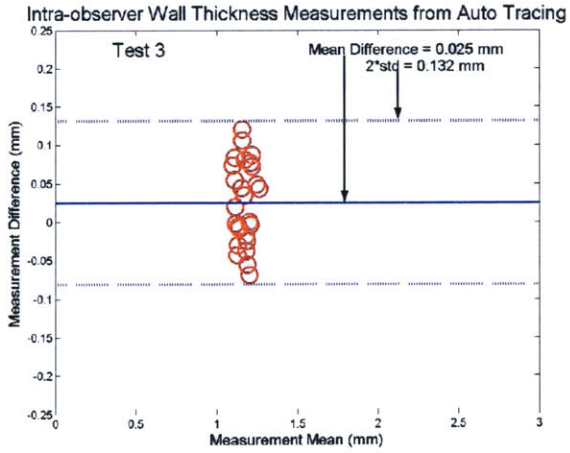

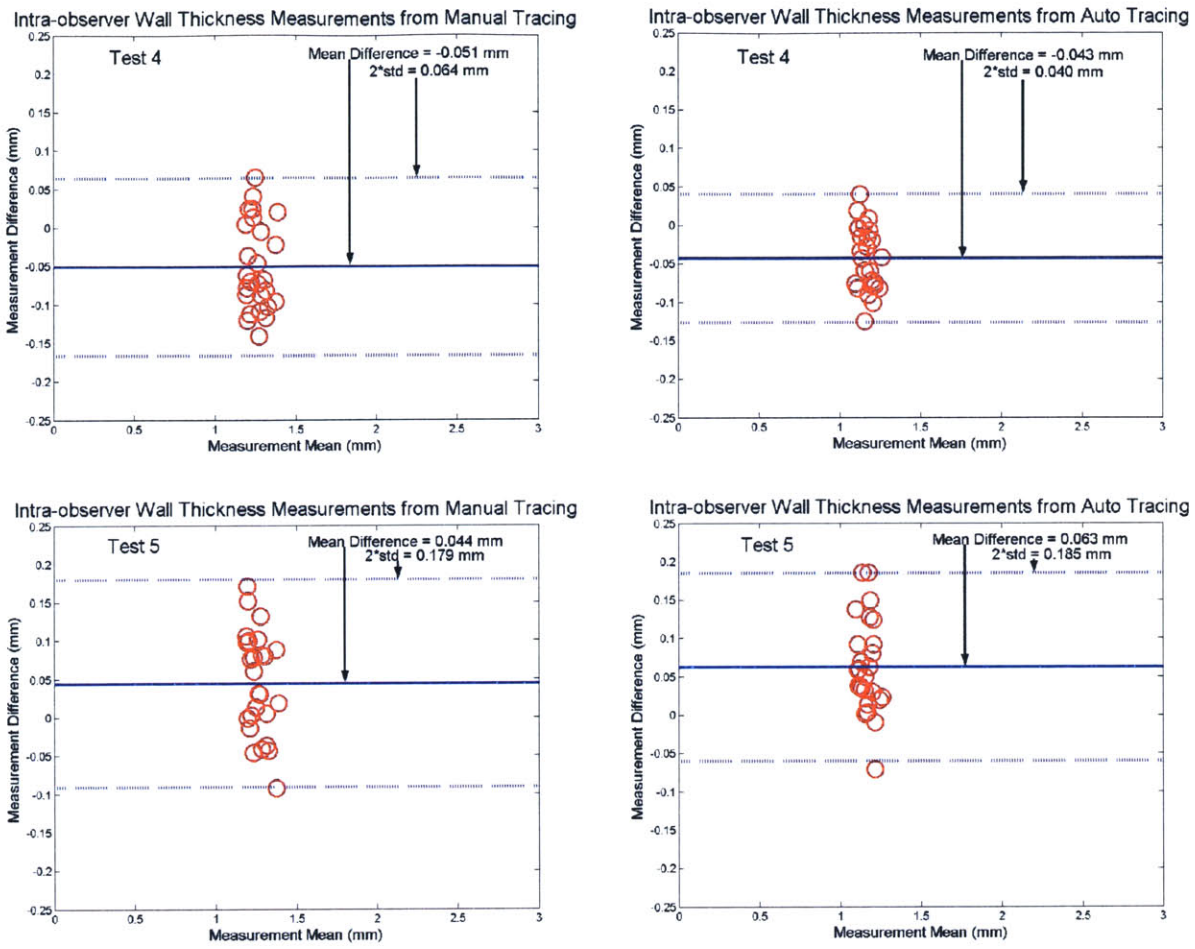

Figure 4-4. Intra-observer results. Bland-Altman plots of intima-media thickness, observer 1, multiple scans. 4-4 A. Manual point selection to determine IMT. 4-4 B. Automatic boundary extraction to determine IMT.

BLAND-ALTMAN				
		Mean IMT (mm)	*Mean IMT Difference (mm)*	*95% Confidence Interval (mm)*
Test 1	***Manual***	1.270	0.010	0.170
	Auto	1.118	-0.048	0.030
Test 2	***Manual***	1.241	-0.019	0.143
	Auto	1.169	0.003	0.108
Test 3	***Manual***	1.276	0.016	0.170
	Auto	1.191	0.025	0.132
Test 4	***Manual***	1.209	-0.051	0.064
	Auto	1.122	-0.043	0.040
Test 5	***Manual***	1.304	0.044	0.179
	Auto	1.228	0.063	0.185

ANDERSON-DARLING TEST				
		Adjusted A^2 test statistic	*Critical value at 95% confidence*	*Null Hypothesis: Accept or Reject*
Test 1	***Manual***	0.568	0.735	Accept
	Auto	0.226	0.735	Accept
Test 2	***Manual***	0.595	0.735	Accept
	Auto	0.297	0.735	Accept
Test 3	***Manual***	0.412	0.735	Accept
	Auto	0.442	0.735	Accept
Test 4	***Manual***	0.704	0.735	Accept
	Auto	0.440	0.735	Accept
Test 5	***Manual***	0.370	0.735	Accept
	Auto	0.486	0.735	Accept

F-TEST			
	F-test statistic	*F-test statistic CDF value*	*Null Hypothesis: Accept or Reject*
Test 1	4.250	0.9997	Reject with 99% Confidence
Test 2	2.397	0.983	Reject with 95% Confidence
Test 3	2.087	0.964	Reject with 95% Confidence
Test 4	1.920	0.945	Reject with 90% Confidence
Test 5	1.222	0.690	Reject with 65% Confidence

Table 4-4. Observer 1, multiple scans. Intra-observer results for Bland-Altman plots, Anderson-Darling normality test and F-test for equivalence of variances.

Intra-Observer: Observer 2 (Inexperienced), Multiple Scans

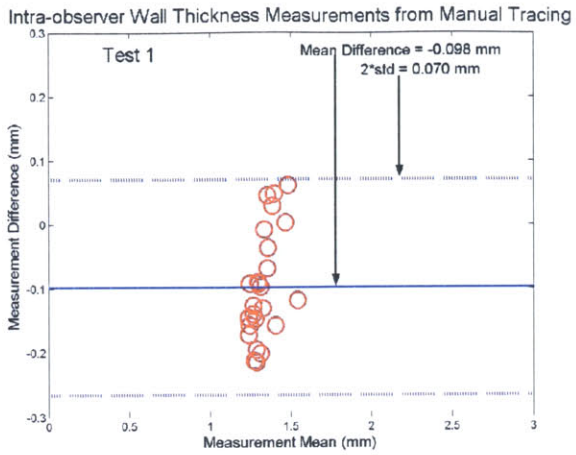

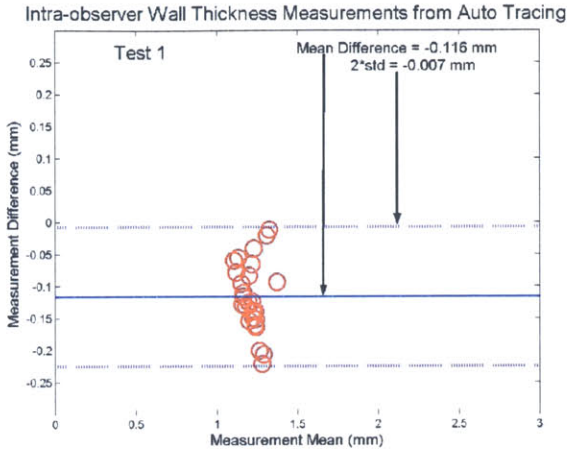

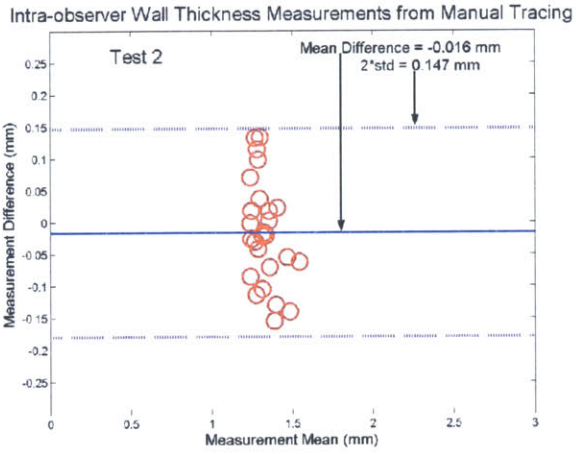

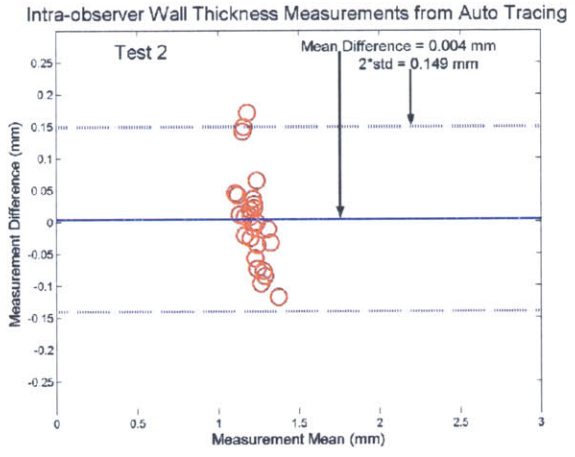

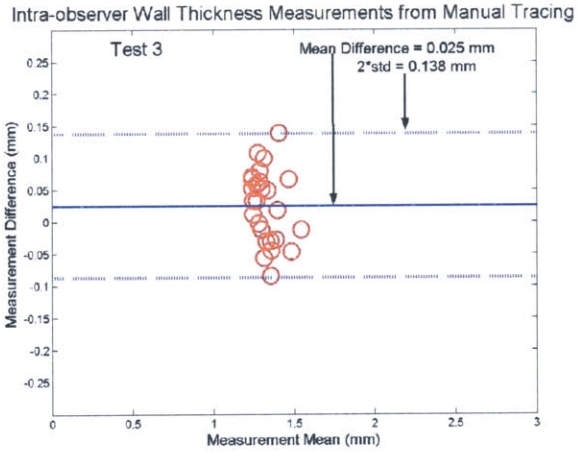

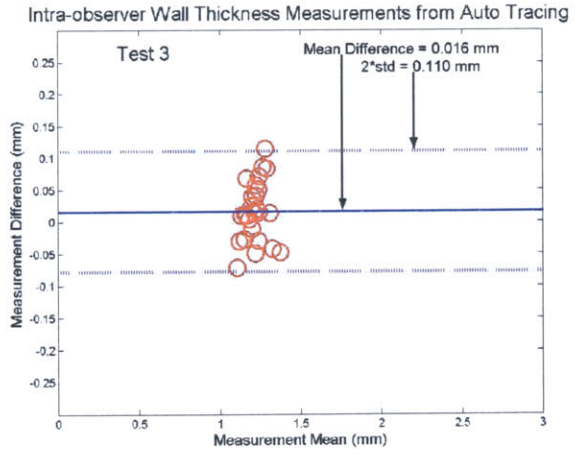

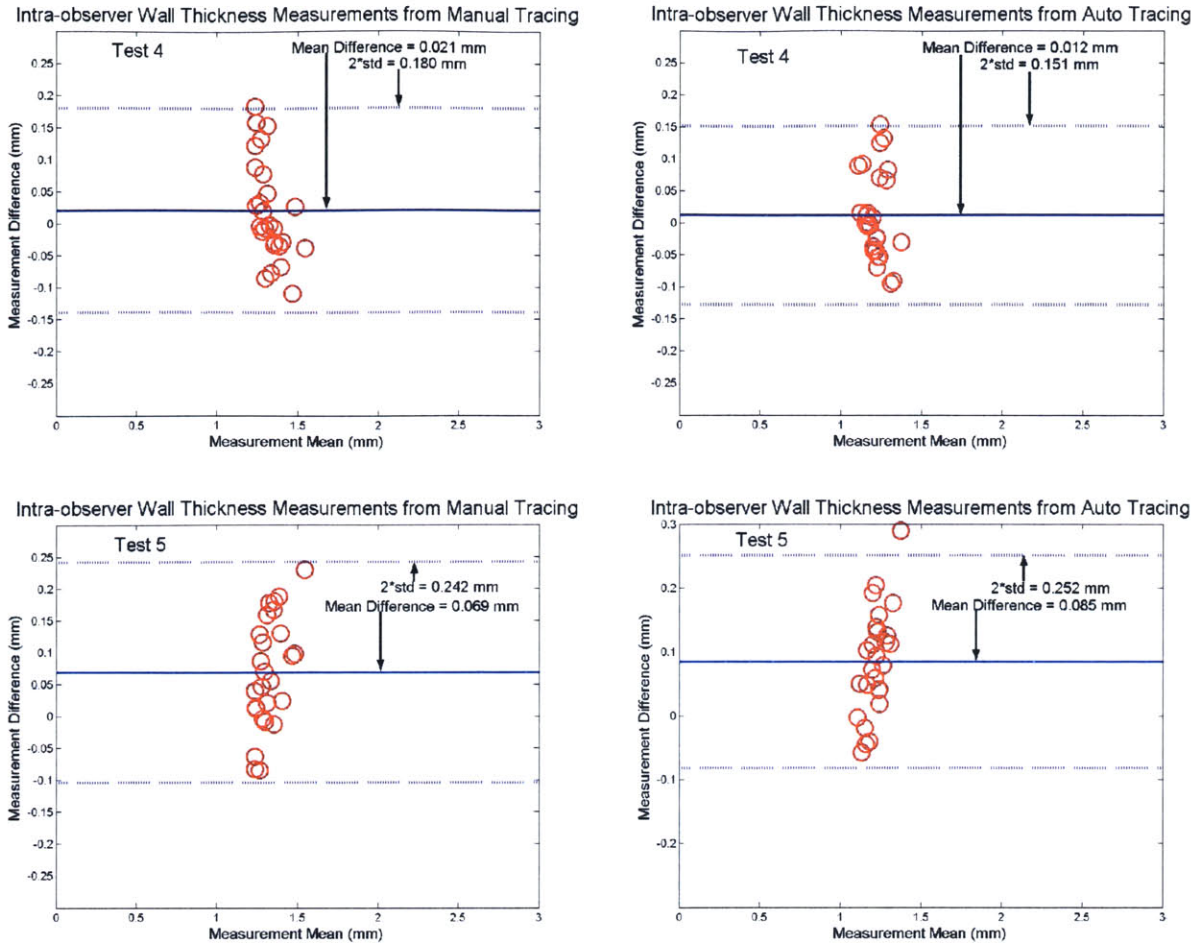

Figure 4-5. Intra-observer results. Bland-Altman plots of intima-media thickness, observer 2, multiple scans. 4-5 A. Manual point selection to determine IMT. 4-5 B. Automatic boundary extraction to determine IMT.

BLAND-ALTMAN				
		Mean IMT (mm)	*Mean IMT Difference (mm)*	*95% Confidence Interval (mm)*
Test 1	***Manual***	1.228	-0.098	0.070
	Auto	1.102	-0.116	-0.007
Test 2	***Manual***	1.309	-0.016	0.147
	Auto	1.222	0.004	0.149
Test 3	***Manual***	1.351	0.025	0.138
	Auto	1.233	0.016	0.110
Test 4	***Manual***	1.346	0.021	0.180
	Auto	1.230	0.012	0.151
Test 5	***Manual***	1.394	0.242	0.069
	Auto	1.303	0.252	0.085

ANDERSON-DARLING TEST				
		Adjusted A^2 test statistic	*Critical value at 95% confidence*	*Null Hypothesis: Accept or Reject*
Test 1	***Manual***	0.786	0.735	Reject
	Auto	0.205	0.735	Accept
Test 2	***Manual***	0.236	0.735	Accept
	Auto	0.545	0.735	Accept
Test 3	***Manual***	0.312	0.735	Accept
	Auto	0.276	0.735	Accept
Test 4	***Manual***	0.553	0.735	Accept
	Auto	0.620	0.735	Accept
Test 5	***Manual***	0.223	0.735	Accept
	Auto	0.169	0.735	Accept

F-TEST			
	F-test statistic	*F-test statistic CDF value*	*Null Hypothesis: Accept or Reject*
Test 1	2.384	0.983	Reject with 95% Confidence
Test 2	1.270	0.722	Reject with 70% Confidence
Test 3	1.433	0.813	Reject with 80% Confidence
Test 4	1.300	0.742	Reject with 70% Confidence
Test 5	1.076	0.572	Reject with 55% Confidence

Table 4-5. Observer 2, multiple scans. Intra-observer results for Bland-Altman plots, Anderson-Darling normality test and F-test for equivalence of variances.

Inter-Observer: Multiple Scans

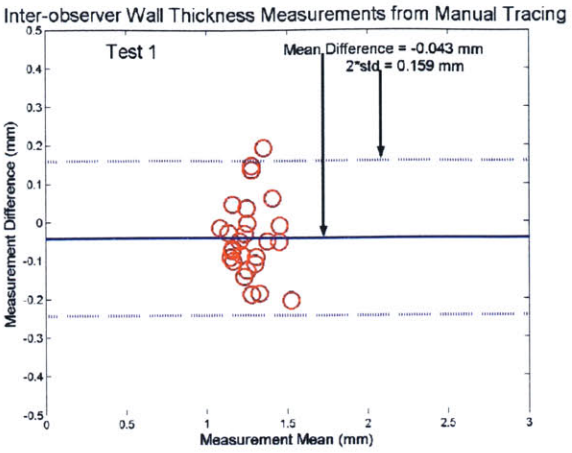

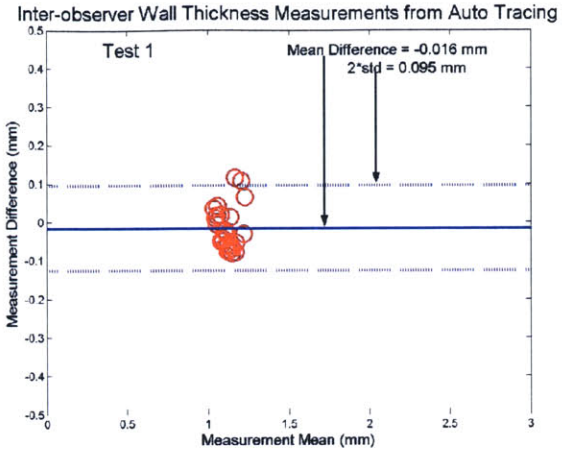

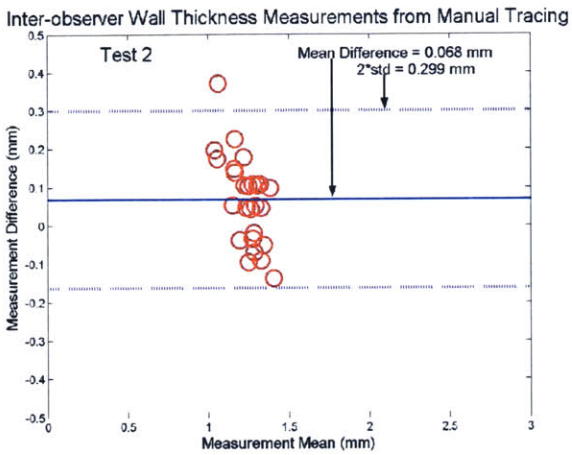

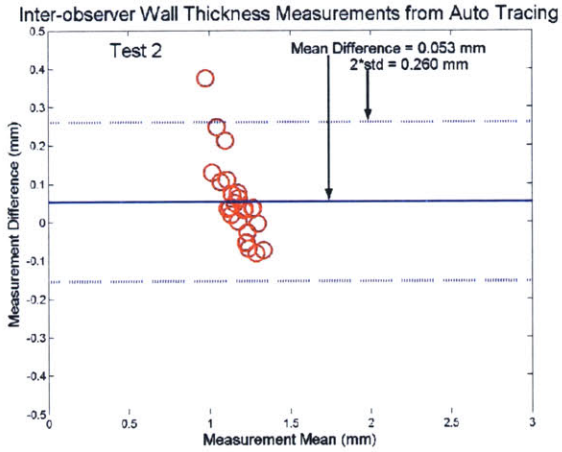

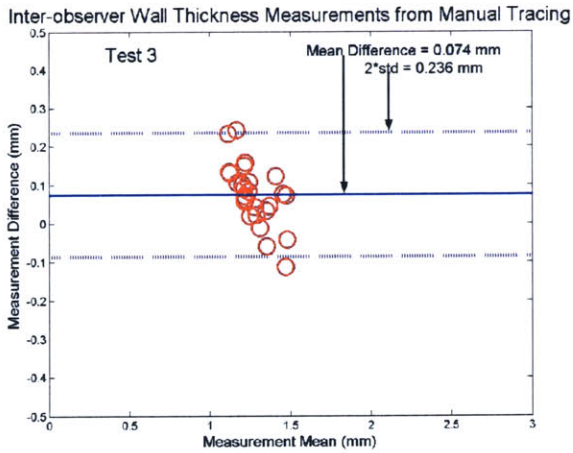

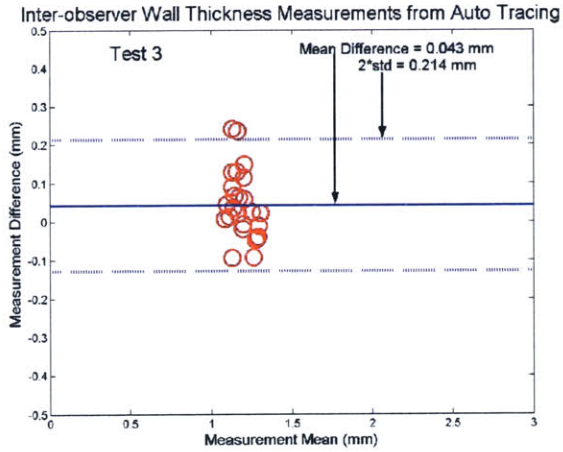

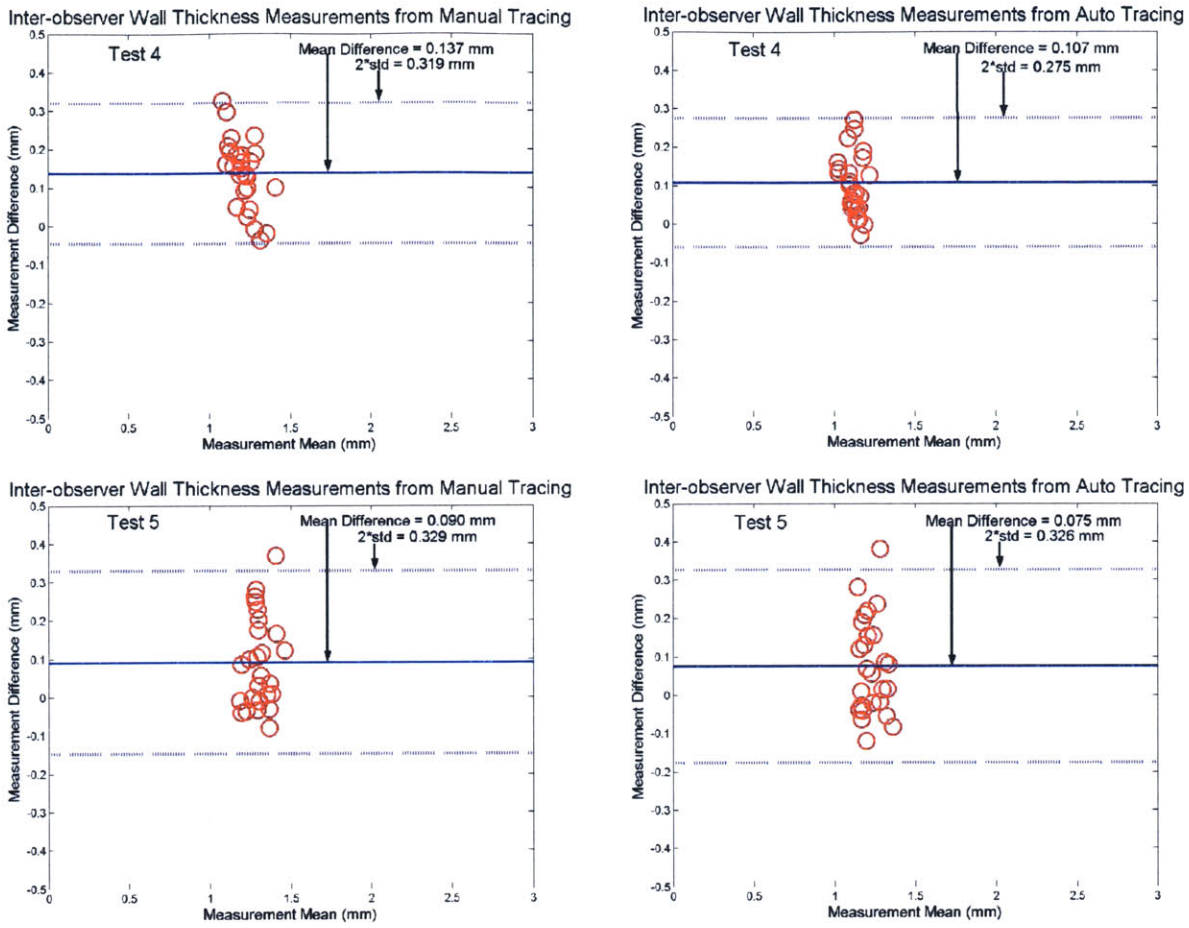

Figure 4-6. Inter-observer results. Bland-Altman plots of intima-media thickness, multiple observers, multiple scans. 4-6 A. Manual point selection to determine IMT. 4-6 B. Automatic boundary extraction to determine IMT.

BLAND-ALTMAN				
		Mean IMT (mm)	*Mean IMT Difference (mm)*	*95% Confidence Interval (mm)*
Test 1	***Manual***	1.228	-0.043	0.159
	Auto	1.102	-0.016	0.095
Test 2	***Manual***	1.309	0.068	0.299
	Auto	1.222	0.053	0.260
Test 3	***Manual***	1.351	0.074	0.236
	Auto	1.233	0.043	0.214
Test 4	***Manual***	1.346	0.137	0.319
	Auto	1.230	0.107	0.258
Test 5	***Manual***	1.394	0.090	0.329
	Auto	1.303	0.075	0.326

ANDERSON-DARLING TEST				
		Adjusted A^2 test statistic	*Critical value at 95% confidence*	*Null Hypothesis: Accept or Reject*
Test 1	***Manual***	0.438	0.735	Accept
	Auto	0.930	0.735	Reject
Test 2	***Manual***	0.354	0.735	Accept
	Auto	1.033	0.735	Reject
Test 3	***Manual***	0.295	0.735	Accept
	Auto	0.487	0.735	Accept
Test 4	***Manual***	0.338	0.735	Accept
	Auto	0.439	0.735	Accept
Test 5	***Manual***	0.657	0.735	Accept
	Auto	0.427	0.735	Accept

F-TEST			
	F-test statistic	*F-test statistic CDF value*	*Null Hypothesis: Accept or Reject*
Test 1	3.283	0.998	Reject with 99% Confidence
Test 2	1.251	0.710	Reject with 70% Confidence
Test 3	1.127	0.617	Reject with 60% Confidence
Test 4	1.172	0.653	Reject with 65% Confidence
Test 5	1.114	0.606	Reject with 60% Confidence

Table 4-6. Inter-observer, multiple scans. Inter-observer results for Bland-Altman plots, Anderson-Darling normality test and F-test for equivalence of variances.

4.3 Sources of Error

For each analysis performed, observers performed an initial manual point selection indicating intima-lumen and media-adventitia boundaries on cross sections of U/S volumes of a carotid vessel. The manual IMT measurements for each of the scans determined from the original point selection by the observer were compared to each other, as were automatic IMT measurements determined by the output of our fully 3D processing scheme. Manual and automatic IMT differences were computed as the slice by slice difference between IMT measurements from separate scans.

For same scan intra-observer tests, one scan of a specimen was analyzed five separate times by an observer. Ideally, the IMT difference between scans would be zero, as the underlying image data was the same for each point selection. Error arises because of the role of the initial point selection in the processing – our automated technique for boundary extraction uses the observer's initial manual point selection as input to the automated technique. Thus differences in the initial point selection will lead to differences in the final boundaries output by the automated processing scheme. Error for inter-observer tests arises for the same reason, as in inter-observer tests two observers are evaluating identical scans. However, in inter-observer tests the error from differences in the initial manual point selection is even more pronounced, as the initial point selection is subject to the bias of the different observers.

For multiple scan intra-observer tests, five separate scans of one specimen were analyzed by an observer and processed through our fully 3D processing scheme. In addition to error arising from differences in the initial point selection as described above, there are three main factors which contribute to non-zero differences in IMT measurements for multiple scan intra-observer tests. The first reason is that while the five scans are of the same specimen, they are separate scans. Factors contributing to the variability between scans include slightly different transducer angles, changes in the position and orientation of the specimen in the specimen holder due to movement of equipment, and changes in the shape of the specimen from slight pressure variations over time. Secondly, each U/S volume being evaluated was voxelized separately, and thus will include some error due to the voxelization process. Third, once the scans have been voxelized they are divided into finite slices to be input into the image processing code. While an attempt was made to reslice the U/S volume from each scan in the same location and orientation,

exact replication between scans could not be achieved as the reslicing process within Stradx is somewhat subjective.

4.4 Discussion

The Anderson-Darling goodness of fit test was used to assess if our IMT difference data sets had a normal distribution. Automatic and manual data sets of the difference in IMT measurements between scans were analyzed using Dataplot software. We see that with only one exception, all IMT difference tests run for Observer 1 (the experienced observer) have an adjusted A^2 test statistic less than the critical value for a normal test at 95% confidence. This indicates that the null hypothesis that the data has a normal distribution can not be rejected. For the tests run on the IMT difference data from Observer 2 (the inexperienced observer), we see a higher number of data sets (5 out of 20) for which we reject the null hypothesis of normality of the data at 95% confidence. However, we note that while the A^2 test statistic for these cases is greater than the critical value at 95% confidence, it is not significantly greater, thus the data set does not deviate significantly from normality. Lastly, for the inter-observer analysis, there is only one test for which the null hypothesis of normality can not be rejected at 95% confidence. For the purposes of further statistical testing, we will assume with a fair degree of confidence that the data sets being tested are normally distributed. Again, it should be noted that the data sets that were tested for normality consisted of the differences in IMT between different point selections, and not the raw IMT results.

Bland-Altman plots of the manual and automatic IMT results show the 95% confidence interval = 2 * standard deviation for each of the tests run. From these plots, we can qualitatively see the difference in the variance between the manual and automatic IMT difference results. To varying degrees of magnitude, we see that the automatic technique for boundary extraction consistently yields more reproducible results than manual point selection, as seen by the smaller variance for the automatic IMT difference results. Quantitative comparison of the variances was performed using the statistical f-test.

The statistical f-test was used to compare the standard deviations of the manual and the automatic data sets. As the f-test tests against the null hypothesis that the variances of the data sets are equal, rejection of the null hypothesis proves that our data sets do *not* have statistically

equivalent variances. In our case, the f-test showed, to varying degrees of confidence, that the IMT results from the automated technique had smaller variances and thus were more reproducible than the manual IMT results. Tables above show the results of the f-test run on each data set of every test. In the table below we see a summary of the average confidence level for rejection of the f-test null hypothesis (and thus the confidence with which we can state that our automatic and manual IMT results have statistically different variances).

	Average Confidence Level for Rejection of F-test Null Hypothesis
Observer 1, Same Scan 1	90%
Observer 1, Same Scan 2	78%
Observer 2, Same Scan 1	76%
Observer 1, Multiple Scans	88.8%
Observer 2, Multiple Scans	74%
Inter-observer, Multiple Scans	70.8%

Table 4-7. Summary of f-test results.

We see that with the experienced observer we generally see a higher confidence level (90%, 78%, and 88.8%) than we do for the inexperienced observer (76% and 74%). Thus for an experienced observer, our fully automated 3D technique for boundary extraction almost always yields more reproducible IMT results than manual point selection. For the inexperienced observer, we see lower confidence levels for rejection of the null hypothesis of the f-test. This is likely due to the fact that the inexperienced observer was performing the initial point selection of the carotid vessel boundaries with no prior experience or training, and only minimal instruction as to what visual clues in the U/S image indicate the location of the vessel boundaries. This adds to the variability in the manual point selection by the inexperienced observer. While the automated technique yielded more reproducible results for vessel wall boundary extraction as measured by IMT than the manual technique, the improvement was not as significant for the inexperienced observer as it was for the experienced observer. This could be due to the lack of training of the inexperienced observer in recognizing the visual clues on the U/S image which indicate the location of the vessel wall adding to the variability in the manual point selection of the vessel boundaries. The results are still promising, as most observers analyzing data in a clinical setting would have some degree of experience and training in visually recognizing the vessel wall boundaries for initial point selection. Also, it is encouraging to note that the

processing scheme as it stands now could still help increase the reproducibility of vessel boundary extraction for any observer, regardless of experience.

We may also look at the difference in results when observers analyze the same scan versus multiple scans of the same specimen. When analyzing one scan multiple times, we isolate the error arising from our automated technique for boundary extraction; when analyzing multiple scans, in addition we must take into account the error of comparing five separate scans, and the error associated with voxelizing five separate scans. In Table 4-7 we see that there is no significant difference in the confidence level for rejection of the null hypothesis when we separate the "same scan" analyses (90%, 78%, and 76% confidence levels) from the "multiple scan" analyses (88.8% and 74% confidence levels). This shows that while the IMT results obtained from multiple scans of the same specimen were more reproducible with the automated technique than with the manual technique, the additional error introduced from taking multiple scans of a specimen is insignificant. This is important to note if we draw a parallel between our experiments and the expected clinical use of this analysis technique. In a clinical setting, we would expect this automated technique for boundary extraction to be used to track changes in a patient's IMT. Scans from the patient taken at different time points would be analyzed and compared – this is comparable to the "multiple scans" analyses where multiple scans of the same specimen were analyzed and compared. It is thus important that the method yields reproducible results when used to analyze scans from multiple time points – if the method is not reproducible over time, we can not confidently compare the IMT results obtained from the technique to assess if a patient has increasing or decreasing IMT. Our results show that this method does in fact yield reproducible results over multiple scans of a specimen, and that the additional error introduced from performing multiple scans of a specimen is small.

The inter-observer test was run to determine the reproducibility of our automated technique for different observers analyzing the same U/S scans. When 2 observers analyzed the same five U/S scans and the results were compared to each other, we saw a 70.8% confidence level for rejection of the f-test null hypothesis. This relatively low level of confidence must be viewed with some reservation, as the inter-observer results were obtained by comparing scans analyzed by an experienced observer to scans analyzed by an inexperienced observer. We have previously shown that the automated results from an inexperienced observer are not as significantly reproducible as results from an experienced observer. Thus we would expect that if

an inter-observer test was run on data sets analyzed by 2 experienced observers, the level of confidence for rejection of the f-test null hypothesis would be greater than 70%. This analysis is important again when we consider the clinical application of this automated boundary extraction technique. When the IMT of a patient is being tracked in a clinical setting, scans may be performed over the course of multiple years. In this time, the same technician may not be available to analyze every scan done on a particular patient, and employees may turn over. It is important that we maintain reproducibility of our results when scans are analyzed by multiple observers. Further analyses must be done with additional experienced observers analyzing U/S volumes to determine the true reproducibility of our automated technique between observers.

Summary and Conclusions

Cardiovascular disease is the leading cause of death in the developed world, and atherosclerosis is the most prevalent form of cardiovascular disease. The slow progression of atherosclerosis provides us with a window of opportunity to halt progression of the disease before an acute clinical event occurs. Initially, atherosclerosis is thought to develop as a response to injury to endothelial cells of the intima. In the early stages of atherosclerosis we see an inflammatory response in the vessel wall. Plaques develop in the vessel wall, and can protrude into the lumen decreasing blood flow downstream. It has been shown that carotid IMT correlates with the presence of cardiovascular disease. It has also been shown that increases in IMT are a marker of underlying atherosclerosis, and are a predictor of future cardiovascular events. Thus we can quantify the progression of disease by tracking changes in IMT.

2D B-mode U/S provides a non-invasive, cost effective means for measuring carotid IMT. Currently, clinical methods for evaluating IMT focus on manual identification of vessel wall boundaries to determine IMT from 2D U/S scans, however a more reproducible method for boundary extraction is desirable. Also, extension of current methods to 3D is crucial as the 2D scans are scan plane dependent, limiting the area over which one can evaluate the progression of the disease. 3D evaluation allows us to more completely characterize disease in a patient.

Chapter 2 describes the equipment and procedure used to acquire the U/S images. Pressure tubing connectors were sutured into the common, internal, and external carotid arteries. The specimen was mounted in a specimen holder and suspended in a shallow saline bath. A saline bag and digital manometer were attached to the plastic tubing connectors so that the internal carotid pressure could be changed and monitored during the scans. The 12-5 MHz peripheral vascular transducer of a Philips Sono CT machine was mounted in a custom built transducer mount so that the transducer could be translated slowly, smoothly, and evenly over the specimen. Stradx software combined with a Flock of Birds was used to capture the images and corresponding 3D position information.

Chapter 3 presents the fully 3D processing scheme used to extract the final vessel wall boundaries. After voxelization of the sequence of 2D U/S images into 3D volumes, our approach applies a fully 3D non-linear, variational energy minimization which uses global voxel information to restore the volume and enhance the inner and outer edge fields. A custom designed technique dubbed DEEE is then applied to the outer edge field to eliminate extraneous

edges still remaining. A 3D deformable surface is applied to the 3D enhanced edge fields together with initial surface locations to extract the final vessel boundaries.

Chapter 4 presents the results of applying our 3D, automated processing scheme to U/S volumes of ex-vivo carotid vessels. We have shown that our automated technique yields more reproducible IMT results than manual point selection for intra- and inter-observer tests. Specifically, for intra-observer tests, the automated method was reproducible for an experienced and an inexperienced observer, although the improvement in reproducibility over manual point selection was not as significant for the inexperienced observer. For inter-observer tests, the automated method yielded a smaller variance in IMT differences than manual point selection, however further tests need to be run comparing the results of two experienced observers to determine the true improvement in reproducibility when using the automated technique.

Bibliography

[1] A. Jemal, T. Murray, et al. Cancer Statistics, 2005. *CA Cancer J. Clin.* **55(1)**, 10-30 (2005).

[2] E. Braunwald. Shattuck lecture – Cardiovascular medicine at the turn of the millennium: Triumphs, concerns, and opportunities. *New Engl. J. Med.* **337(19)** 1360-1370 (1997).

[3] P. Pignoli, E. Tremoli, et al. Intimal plus medial thickness of the arterial wall: a direct measurement with ultrasound imaging. *Circulation* **74(6)**, 1399-1406 (1986).

[4] American Heart Association, www.americanheart.org, February 25, 2005.

[5] American Heart Association, "Heart and Stroke Facts." www.americanheart.org 2003.

[6] F.J. Schoen and R.S. Cotran. "Blood Vessels," in *Robbins Pathologic Basis of Disease, 6th edition.* R.S. Cotran, V. Kumar, and T. Collins, Eds., 493-541. W.B. Saunders Company, Philadelphia, PA, 1999.

[7] J.A. Jensen. *Estimation of Blood Velocities Using Ultrasound: a Signal Processing Approach.* Cambridge University Press, Cambridge, Great Britain, 1996.

[8] E.T.H. Yeh. CRP as a Mediator of Disease. *Circulation* **109(suppl II)**, II-11--II-14 (2004).

[9] D. Steinberg. Atherogenesis in perspective: Hypercholesterolemia and inflammation as partners in crime. *Nature Medicine* **8(11)**, 1211-1217 (2002).

[10] T.A. Pearson, G.A. Mensah, et al. Markers of inflammation and cardiovascular disease: Application to clinical and public health practice. *Circulation* **107**, 499-511 (2003).

[11] R. Ross, and J.A. Glomset. The pathogenesis of atherosclerosis (second of two parts). *New Engl. J. Med.* **295(8)** 420-425 (1976).

[12] R. Ross. The pathogenesis of atherosclerosis: a perspective for the 1990s. *Nature* **362(6423)** 801-809 (1993).

[13] R. Ross. The pathogenesis of atherosclerosis – an update. *New Engl. J. Med.* **314(8)** 488-500 (1986).

[14] R. Ross. Atherosclerosis: an inflammatory disease. *New Engl. J. Med.* **349(2)** 115-126 (1999).

[15] K. Wattanakit, A.R. Folsom, L.E. Chambless, and F.J. Nieto. Risk factors for cardiovascular event recurrence in the Atherosclerosis Risk in Communities (ARIC) study. *Am. Heart J.* **149(4)** 606-612 (2005).

[16] A.J. Taylor, L.E. Sullenberger, H.J. Lee, J.K. Lee, and K.A. Grace. Arterial Biology for the Investigation of the Treatment Effects of Reducing Cholesterol (ARBITER) 2. *Circulation* **110** 3512-3517 (2004).

[17] Z.A. Fayad, and V. Fuster. Clinical Imaging of the High-Risk or Vulnerable Atherosclerotic Plaque. *Circ. Res.* **89** 305-316 (2001).

[18] A. Fenster, D. Downey, and H.N. Cardinal. Three-dimensional ultrasound imaging. *Phys. Med. Biol.* **46**, R67-R99 (2001).

[19] A. Landry, J.D. Spence, and A. Fenster. Measurement of carotid plaque volume by 3-dimension ultrasound. *Stroke* **35**, 864-869 (2004).

[20] R.W. Prager, R.N. Rohling, A.H. Gee and L. Berman. Automatic calibration for 3-D free-hand ultrasound. Technical report CUED/F-INFENG/TR 303, Cambridge University Department of Engineering, September 1997.

[21] B.M. Dawant and A.P. Zijdenbos. "Image Segmentation" in *Handbook of Medical Imaging, Volume 2: Medical Image Processing and Analysis.* M. Sonka and J.M. Fitzpatrick, Eds., 71-127. SPIE Press, Bellingham, WA, 2000.

[22] P.A. Mlsna and J.J. Rodriguez. "Gradient and Laplacian-Type Edge Detection" in *Handbook of Image & Video Processing.* A. Bovik, Ed., 415-431. Academic Press, San Diego, CA, 2000.

[23] C. Xu, D.L. Pham, and J.L. Prince. "Image Segmentation Using Deformable Models" in *Handbook of Medical Imaging, Volume 2: Medical Image Processing and Analysis.* M. Sonka and J.M. Fitzpatrick, Eds., 129-174. SPIE Press, Bellingham, WA, 2000.

[24] M. Kass, A. Witkin, and D. Terzopoulos. Snakes: Active Contour Models. *Int. J. Comp. Vision* 321-331 (1988)

[25] J. Shah. "A common framework for curve evolution, segmentation and anisotropic diffusion," in *Proceedings 1996 IEEE Computer Society Conference on Computer Vision and Pattern Recognition,* San Francisco, CA, USA, Proceedings of IEEE Conference on Computer Vision and Pattern Recognition, 136-142, IEEE Comput. Soc. Press. (1996)

[26] R.C. Chan. Non-invasive ultrasound monitoring of regional carotid wall structure and deformation in atherosclerosis. Doctoral dissertation, Massachusetts Institute of Technology, 77 Massachusetts Ave., Cambridge MA, May 2001.

[27] J. Kaufhold. Energy formulations of medical image segmentations. Doctoral dissertation, Boston University, 2000.

[28] W. Clem Karl. "Regularization in Image Restoration and Reconstruction" in *Handbook of Image & Video Processing.* A. Bovik, Ed., 141-160. Academic Press, San Diego, CA, 2000.

[29] *NIST /SEMATECH e-Handbook of Statistical Methods*, http://www.itl.nist.gov/div898/handbook/prc/section2/prc213.htm, March 24, 2005.

[30] *NIST / SEMATECH e-Handbook of Statistical Methods*, http://www.itl.nist.gov/div898/handbook/eda/section3/eda359.htm, March 24, 2005.

[31] J.M. Bland and D.G. Altman. Statistical methods for assessing agreement between two methods of clinical measurement. *Lancet* **i** 307-310 (1986).